Key Points:
- Geostationary Operational Environmental Satellite-16 (GOES-R) derived atmospheric motion vector (AMV) product has the potential to benefit convective scale data assimilation and forecasts
- The impact of assimilating GOES-R derived AMVs on short-range severe thunderstorm forecasts is evaluated
- The short-range forecasts of three severe weather events are improved by AMV DA compared to the control experiment without any observations

Correspondence to:
J. Gao,
jidong.gao@noaa.gov

Impact of Assimilating High-Resolution Atmospheric Motion Vectors on Convective Scale Short-Term Forecasts. Part II: Assimilation Experiments of GOES-16 Satellite Derived Winds

Juan Zhao[1,3] , **Jidong Gao[2,4]** , **Thomas Jones[3,2,4]**, and **Junjun Hu[3,2]**

[1]China Meteorological Administration Training Centre, Beijing, China, [2]NOAA/National Severe Storms Laboratory, Norman, OK, USA, [3]Cooperative Institute for Mesoscale Meteorological Studies, The University of Oklahoma, Norman, OK, USA, [4]School of Meteorology, The University of Oklahoma, Norman, OK, USA

Abstract Building on the results from the observing system simulation experiments in Part I, this study investigates the impact of assimilating Geostationary Operational Environmental Satellite-16 (GOES-16) derived atmospheric motion vector (AMV) data on the convective scale numerical weather prediction (NWP) by using the National Severe Storms Laboratory (NSSL) three-dimensional variational (3DVAR) data assimilation (DA) system. The benefit of the AMV DA for short-term severe weather forecast is assessed with three high-impact weather events that occurred in spring 2018 and 2019 over the Great Plains of the United States. The results show that the wind and equivalent potential temperature fields associated with the storm environment and the nearby ongoing convection are improved by the AMV DA, which yields better simulation of the boundaries and the subsequent forecasts of storm evolution. For the quasi-linear or mesoscale convective system, the assimilation of AMVs has a positive impact on the 0–3 h forecasts of composite reflectivity and accumulated precipitation in terms of the shape, location, and magnitude. However, the AMV DA has difficulty in capturing the sharp moisture gradient associated with the dryline and mostly underpredicts the associated scattered storms.

Plain Language Summary The high-spatiotemporal-resolution atmospheric motion vectors (AMVs) derived from newly launched Geostationary Operational Environmental Satellites-16/17 (GOES-16/17; also named GOES East/West) may have the potential to improve short-range severe weather forecasts. However, this has not been extensively explored. In this study, a three-dimensional variational data assimilation scheme developed at NOAA/National Severe Storms Laboratory and the Weather Research and Forecasting model are used to investigate the impact of assimilating GOES-R derived AMVs on short-range severe thunderstorm forecasts. It is demonstrated that, compared to the control experiment without assimilating any observations, the short-range forecasts of the quasi-linear or mesoscale convective systems in three severe weather events are all improved based on verification against radar reflectivity and precipitation observations when assimilating the AMV data.

1. Introduction

New-generation geostationary satellites, such as Geostationary Operational Environmental Satellites-16/17 (GOES-16/17), Himawari-8/9, Geostationary Korea Multipurpose Satellite-2A (GEO-KOMPSAT-2A/2B), EUMETSAT-Meteosat Third Generation, and Fengyun-4, and so on, can provide high-spatiotemporal-resolution atmospheric motion vector (AMV) products containing mesoscale or convective flow information. Recent studies showed that assimilating high-resolution AMVs has generally slightly positive or neutral impacts on the global and regional model analyses and forecasts, especially with small reductions in wind errors (Cherubini et al., 2006; Elsberry et al., 2018; James & Benjamin, 2017; Kim & Kim, 2018; Kim et al., 2017; Le Marshall et al., 2008; Lean et al., 2016; Lean & Bormann, 2019; Li et al., 2020; Lim et al., 2019; Mallick & Jones, 2020; Otsuka et al., 2015; Sawada et al., 2019; Velden et al., 2017; Wu et al., 2015; Yamashita, 2012, 2017). Most of these studies focused on improving the hurricane, or tropical cyclone track and intensity forecasts by assimilating high-density or rapid-scan AMVs into a variational data assimilation (DA) or ensemble-based Kalman filter framework. However, the impact of high-spatiotemporal-resolution AMVs on mesoscale and convective scale weather forecasts over land has not been extensively explored (e.g., Mallick

& Jones, 2020). The main purpose of this two-part study is to investigate the impact of high-resolution AMVs on convective scale DA and numerical weather prediction (NWP).

In Part I of this two-part study, the impact of assimilating high-resolution AMVs on convective scale NWP is evaluated using simulated data of an idealized supercell storm. The results of the baseline DA experiment demonstrate that the errors in wind and other model variables are reduced by assimilating the simulated AMVs, leading to the enhancement of the storm-top divergence and low-level convergence, and the low-level cold pool associated with the simulated supercell storm. Three sets of sensitivity experiments are also performed to test the impact of observation resolution, DA cycling frequency, and horizontal correlation length scale, respectively. Overall, assimilating higher-spatial-resolution AMVs at higher cycling frequency results in better initial conditions and storm forecasts, except that the experiment with the most frequent DA cycling (5-min interval) tends to overestimate temperature, nonprecipitating hydrometeor, and storm-relative helicity fields, and produce spurious cells in the short-term forecasts. It is also found that the correlation length scale length of 20 km produces the best forecasts. These conclusions will serve as a reference guide for the assimilation of real-time AMV data.

The Advanced Baseline Imager (ABI) aboard the GOES-16/17 (Schmit et al., 2005, 2017) brings an opportunity for retrieving high spatiotemporal-resolution AMVs over the Continental United States (CONUS), which can better monitor the mesoscale or convective scale atmospheric flow. However, the benefit of these data for convective scale NWP has not yet been extensively explored (Daniels et al., 2012). Therefore in Part II of this two-part research, the value of assimilating GOES-16 ABI derived AMVs data on high-impact weather events in a real scenario is assessed with the same 3DVAR DA system used in Part I (Gao et al., 2004, 2013). Although the encouraging results obtained in the idealized case study suggested that the simulated high-resolution AMVs have a positive impact on convective scale DA and storm forecasts, the influence of the AMV observations in the real data cases may be different depending on observation quality and distribution. As with the simulated data, the AMVs are confined to the region and vertical layer where the targeted tracers exist. There could be large areas without data, or there may be few data in the region where more information about mesoscale and convective flows is needed. The acceptable height range of AMVs and the corresponding data quality depend on the retrieving band (Daniels et al., 2012), which should be considered in the quality control strategy. Still, as demonstrated in Part I, the storm morphology and evolution are sensitive to the wind fields, the impact of AMV DA on severe storm forecasts can be very useful depending on different weather situations.

Since the forecast model and the 3DVAR system have been described in Part I of this study, only the main points are briefly summarized and the refinement in the quality control (QC) and assimilation settings for the GOES-16 derived AMVs, as well as the experimental design, are presented in Section 3. In Section 4, the results of the three real data cases are discussed. Finally, the summary and conclusions are offered in Section 5.

2. Brief Description of GOES-16 AMV Data

AMVs in prepbufr format are post-processed for use in the operational models, however, they contain wind observations at a much coarser spatial and temporal resolution, which is not suitable for convective scale NWP. As indicated in Part I, this study uses the GOES-16 ABI Level 2 (L2) AMV product generated by NOAA NESDIS Center for Satellite Applications and Research (https://www.bou.class.noaa.gov/saa/products/search?sub_id=0&datatype_family=GRABIPRD&submit.x=15&submit.y=6) in NetCDF file format. The ABI aboard the GOES-16/17 satellites offers 11 more bands and has four times the spatial resolution and more than three times faster scanning ability than its predecessor aboard the GOES-N series (Daniels et al., 2012; Goodman et al., 2012; Schmit et al., 2005, 2017). The ABI AMV product is generated from a set of targeted tracers, including cloud edges or moisture gradients, viewed separately in each of six selected spectral channels: bands 2 (0.64 µm), 7 (3.9 µm), 8 (6.15 µm), 9 (7.0 µm), 10 (7.4 µm), and 14 (11.2 µm). Table 1 lists the band number, central wavelength, tracer type, and temporal coverage for different ABI bands used to derive AMVs. Generally, AMVs are retrieved for cloudy and cloud-free, daylight and nightlight conditions depending on the band. For example, the visible AMVs (band 2) are only available during the

Table 1
List of the ABI Bands Used to Derive AMVs

ABI band	Central wavelength (μm)	Tracer type	Temporal coverage	Acceptable height range (hPa)
2	0.64	Cloud	Day	700–1,000
7	3.9	Cloud	Night	700–1,000
8	6.15	Cloud/Clear-sky water vapor	Day and night	100–400
9	7.0	Clear-sky water vapor	Day and night	100–1,000
10	7.4	Clear-sky water vapor	Day and night	450–700
14	11.2	Cloud	Day and night	100–1,000

Note. From left to right column, ABI band number, central wavelength, tracer type, temporal coverage, and acceptable height range.

daytime while the AMVs from shortwave infrared band 7 are produced during the nighttime. Nevertheless, both cloud and clear-sky water vapor-based AMV products are generated for band 8 (Table 1).

The ABI native spatial resolutions at nadir are 2 km for the infrared bands and 0.5 km for the 0.64-μm visible band. The spatial resolution of AMV data, which is coarser than the ABI native spatial resolution, is determined by both the spatial and temporal resolution of the ABI imagery and the scale of the intended feature being tracked (Daniels et al., 2012; Hamada, 1983; Shenk, 1991). For example, the horizontal resolution of the visible AMVs (derived from visible band 2) is 7.5 km, while the resolution of the wind data from the water vapor bands (bands 8–10) and longwave infrared band (band 14) is 30 and 38 km, respectively (Daniels et al., 2012). To account for the error in AMV height assignment by the retrieving algorithm, the vertical resolution of AMV product is quite sparse, with only three layers: 1,000–700, 700–400, and 400–100 hPa (Rao et al., 2002), and the acceptable height range depends on the retrieving band (Table 1). Most studies show that the vertical distribution of the multispectral winds exhibits a typical bimodal pattern with maximums in the upper and lower troposphere, which is determined by the nature of the derivation algorithm (Goerss et al., 1998; Lean & Bormann, 2019; Nebuda et al., 2014; Xiao et al., 2002). Moreover, assigning a height to the targeted tracer is often considered to be the major uncertainty for AMVs (Velden & Bedka, 2009). Previous studies revealed that the AMVs height assignment error is the largest in the middle level (700–400 hPa) and smallest in the upper level (400–100 hPa; Lean & Bormann, 2019; Salonen et al., 2015).

In terms of the temporal resolution, the GOES-16 AMVs are available once an hour for the Full Disk (FD) of the Earth, every 15 min over the CONUS region, and every 5 min over a selectable 1,000 by 1,000 km mesoscale sector box (MESO). Following the conclusions from DA cycling frequency sensitivity experiment in Part I, the 15-min AMV data over the CONUS scan sector is chosen to be assimilated in this study. Owing to higher temporal, spatial and spectral resolution, as well as increased radiometric performance of the GOES-16 ABI, the retrieval algorithm is improved in the presence of better target selection, feature tracking, and target height assignment, resulting in higher quality AMV observations as a better representation of the low-level visible winds over land (Daniels et al., 2012; Lean & Bormann, 2019). Therefore, it is expected that assimilating the high-spatiotemporal-resolution AMVs will introduce mesoscale or convective scale airflow features into analysis and consequently improve the accuracy of severe storm forecasts over CONUS.

3. Forecast Model, Data Quality Control, and Experimental Design

3.1. Forecast Model

The forecast model used in this study is the fully compressible, non-hydrostatic Advanced Research version of the Weather Research and Forecasting (WRF-ARW) Model version 3.6.1 (Skamarock et al., 2008). The DA and forecast experiments are performed on one single domain with a horizontal spatial resolution of 1.5 km and horizontal dimensions of 600×600 grid points. The simulation domains from the Warn-on-Forecast System (WoFS) real-time Spring Forecast Experiment (SFE) runs are employed for all three cases in this study (Hu et al., 2020). There are 51 stretched vertical levels with a model top set at 20-hPa. For the physical parameterizations, we select the National Severe Storms Laboratory (NSSL) two-moment four-ice category

bulk microphysics scheme (Mansell et al., 2010; Mansell & Ziegler, 2013; Ziegler, 1985), the Rapid Radiative Transfer Model (RRTM) longwave radiation scheme (Mlawer et al., 1997), the Dudhia shortwave radiation scheme (Dudhia, 1989), the Rapid Update Cycle (RUC) land surface scheme (Benjamin et al., 2004), and the Yonsei University (YSU) planetary boundary layer scheme (Hong et al., 2006).

3.2. Data Quality Control and Assimilation Setting

Following Part I of this study, this work employs the NSSL Experimental WoF 3DVAR system (NSSL3D-VAR; Gao et al., 2013, 2016; Gao & Stensrud, 2012, 2014). The NSSL3DVAR system is capable of effectively assimilating radar reflectivity, radial velocity, satellite-derived cloud water path, and total precipitable water, Geostationary Lightning Mapper (GLM)-derived water vapor, sounding, and surface data (Fierro et al., 2019; Hu et al., 2019, 2020; Lai et al., 2019; Pan et al., 2018). In this study, the QC and assimilation modules for the GOES-16 AMVs are built into the NSSL3DVAR system, which will be described in more detail later in this section.

As mentioned above, this work assimilates ABI L2 AMV data from GOES-16 over the CONUS region. The raw observations of wind speed and azimuth from the AMV data sets are converted to zonal and meridional wind components (u and v) before entering the NSSL3DVAR system. To make full use of the mesoscale and convective scale airflow information, no data thinning is employed in this study. The wind observations are passed through a QC module to filter out bad data, before their insertion into the analysis procedure. Based on the channel-dependent pressure ranges for AMVs (Daniels et al., 2012) and the QC strategy adopted by previous studies (Kim et al., 2017; Lim et al., 2019; Mallick & Jones, 2020; Sawada et al., 2019; Velden et al., 2017), the seven-step observation checks depending on retrieval band are applied as the following:

1. Remove all the wind data from the surface to 950 hPa and that above 100 hPa;
2. For the winds derived from both visible (0.64 μm) and shortwave infrared (3.9 μm) bands, remove data above 750 hPa;
3. For the upper-level water vapor winds (6.15 μm), reject data below 400 hPa;
4. For band 9 (7.0 μm) winds, keep the data above 450 hPa only and with a minimum wind speed threshold of 8 m/s;
5. For the longwave infrared band (11.2 μm), remove winds retrieved between 800 and 400 hPa;
6. Reject all the data with a solar zenith angle larger than 68°; and
7. A relaxed gross error check, which is designed to increase the retention of winds representing smaller-scale flow, is performed to eliminate the observations outside of set tolerances from the interpolated model background field. Similar to Mallick and Jones (2020), the threshold value between the ratio of the innovation to the observation error is set to 5.

The above QC checks generally filter out 20%–30% of the available AMV observations in each analysis cycle. As in Part I of this study, the observation and background error for wind components are set to be 6 and 3–6 m/s, respectively. This study adopts the minimization process in two loops, each with a prescribed horizontal and vertical correlation scale for the recursive filter used in the program (Gao et al., 2004; Purser et al., 2003). The correlation scales determine how far the observation information will spread in model space. Following the sensitivity experiment results in Part I, the horizontal correlation scale lengths are set to be 50 km in the first loop and 20 km in the second loop. And the corresponding vertical correlation lengths are 7 and 5 grid points, respectively.

3.3. Experimental Design

The assimilation of GOES-16 ABI L2 AMV data is performed with three high-impact weather events that occurred over the Great Plains of the United States in spring 2018 and 2019. The DA and forecast cycle workflow, similar to that of WoFS real-time SFE runs (Hu et al., 2020; Jones et al., 2018), is utilized for each real case (Figure 1). The WRF model is initialized with the 3-km High Resolution Rapid Refresh (HRRR) forecast product at 1800 UTC, which is downscaled onto the 1.5-km grid. Then the AMV DA is cycled from 1800 to 0300 UTC at 15-min intervals, with a 3-h free forecast launched every hour starting from 1900 UTC. The GOES-16 AMV data passing all QC checks between $t-10$ and $t+5$ min are accumulated and assimilated at each analysis time t. A control run (denoted as NoDA) is also performed by integrating the model
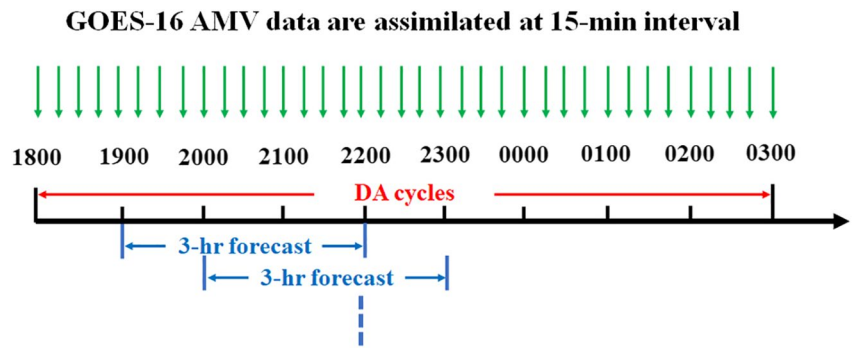
Figure 1. Illustration of the data assimilation and forecast cycle workflow. A 3-h forecast is launched every hour from 1900 to 0300 UTC (namely, nine separate forecasts).

forward without assimilating any observation and is compared to the AMV DA experiment (referred to as AMV).

To obtain both qualitative and quantitative evaluations of the AMV DA impact on the analyses and forecasts, the root-mean-square errors (RMSEs) and biases of wind components against the AMV data during the DA cycles are calculated first. Then, the model reflectivity and precipitation fields are verified against the composite radar reflectivity observations from the NSSL Multi-Radar Multi-Sensor (MRMS) product (Smith et al., 2016) and the Stage IV hourly rainfall estimates from the National Centers for Environmental Prediction (Baldwin & Mitchell, 1997), all of which are interpolated onto the 1.5-km model grids by using the bilinear interpolation method for the convenience of comparing observations to model simulations. Specifically, the verification parameters include the probability of detection (POD), the false alarm rate (FAR), success ratio (SR), and critical success index (CSI), and neighborhood-based scores like the equitable threat scores (ETS; Clark et al., 2010) and the fractions skill scores (FSS; Roberts & Lean, 2008).

4. Results

The three high-impact weather events that occurred over the Great Plains of the United States on May 1, 2018, May 28, 2019, and May 17, 2019 produced distinct storm modes under different weather situations. Numerous severe weather warnings were issued by the National Weather Service (NWS) for all three cases with subsequent storm reports including large hail, damaging winds, and tornadoes. In addition to the wind and equivalent potential temperature analyses, the short-term (0–3 h) forecasts of composite reflectivity and accumulated precipitation are discussed.

4.1. Case 1: May 1, 2018

During the late afternoon and the evening of May 1, 2018, a southwest-northeast slow-moving cold front arcing across west-central Kansas into eastern Nebraska moved northeastward with a surface low over Kansas. Owing to the favorable environmental conditions, clustered storms developed near the low pressure and along the front through the night and finally merged into a quasi-linear convective system, squall line (not shown). Between 2300 UTC May 1 and 0200 UTC May 2, a total of 13 tornadoes and several large hail and damaging wind events were reported in Kansas, Nebraska, and Oklahoma. Moreover, a couple of discrete storms initiated along a dryline extending southward from the front.

Figures 2a–2d display the geographical distribution of AMV data assimilated at 1800 and 2100 UTC May 1 as well as 0000 and 0300 UTC May 2, 2018. It is seen that AMVs within the 400–100 hPa layer greatly outnumber the wind vectors below 400 hPa. This occurs because the majority of winds are retrieved from the upper-level water vapor band (6.15 μm) which represent upper-level cirrus cloud movements. A few AMVs from longwave infrared band (11.2 μm) are also derived within this layer. Diffluent flow within the 400–100 hPa layer is apparent at the periphery of the squall line as it moved northeastward (Figures 2b–2d). The upper-tropospheric divergence signature is a good measure of the updraft velocity and plays an
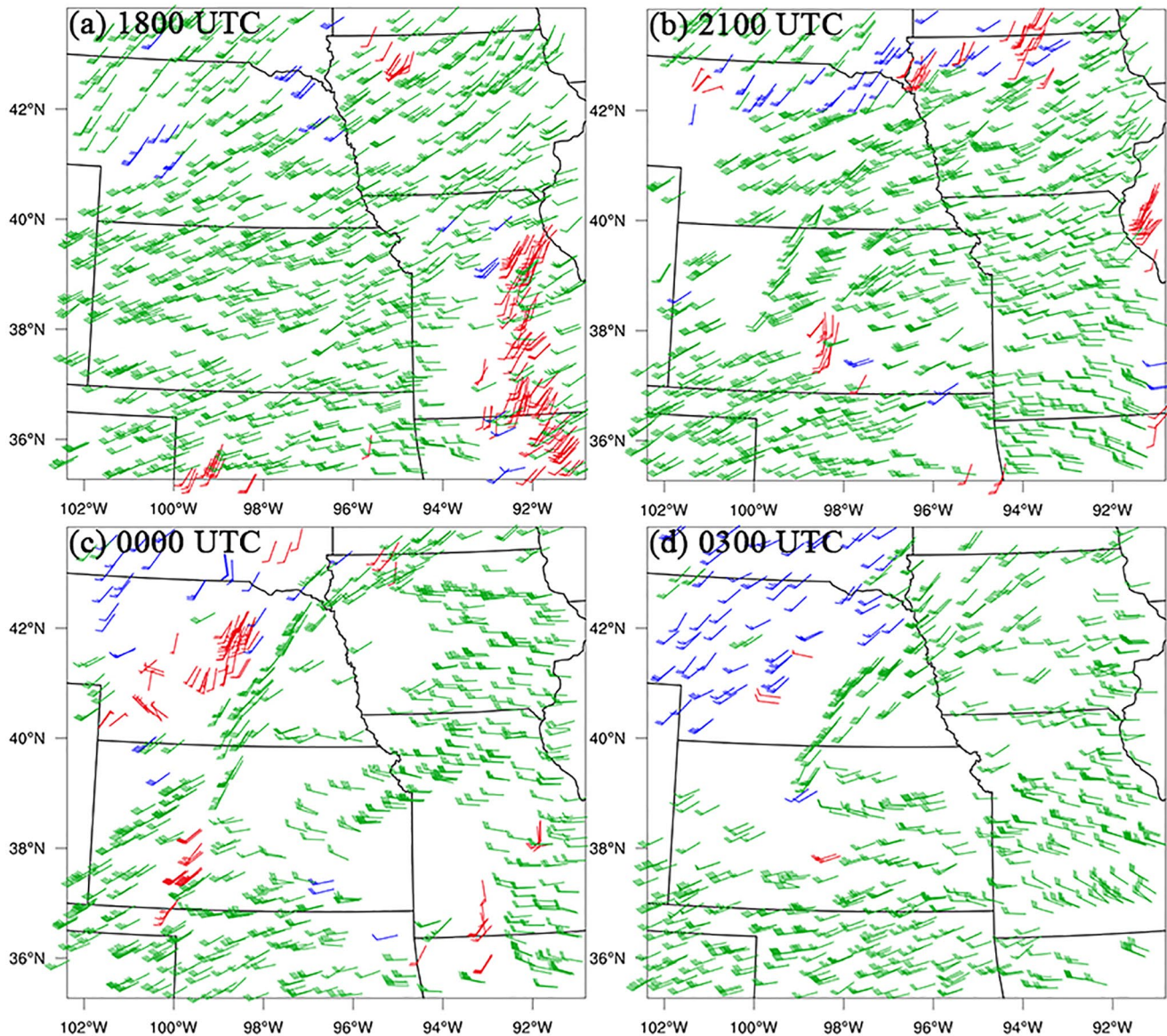
Figure 2. The geographical distribution of the GOES-16 atmospheric motion vector (AMV) observations which are assimilated at (a) 1800 UTC May 1, (b) 2100 UTC May 1, (c) 0000 UTC May 2, and (d) 0300 UTC May 2, 2018. Red barbs represent AMVs within the 1,000–700 hPa layer, blue AMV barbs are within the 700–400 hPa layer, and green AMV barbs are within the 400–100 hPa layer.

important role in initiating convective storm development and maintaining storm intensity (Doswell, 2001). The low-level cyclonic wind shear behind the cold front is evident within the 1,000–700 hPa layer over the central Nebraska (Figure 2c).

The RMSEs and biases for the wind background and analyses against the GOES-16 AMV data during the DA cycles are shown in Figures 3a and 3b. The analyzed RMSEs are significantly smaller than those from the background throughout all the assimilation cycles (Figure 3a). This indicates the analysis is closer to the observations than the background, which confirms that the 3DVAR system generally ingests all the available observations reasonably well. And the biases for both wind components are improved (closer to zero) when AMV data are assimilated (Figure 3b). The RMSEs for u and v components are also computed and aggregated over nine 3-h free forecasts launched every hour from 1900 to 0300 UTC (Figure 3c). The forecast errors generally increase with integration time and the benefit of assimilating AMV is obvious in the first two hours into the forecasts.
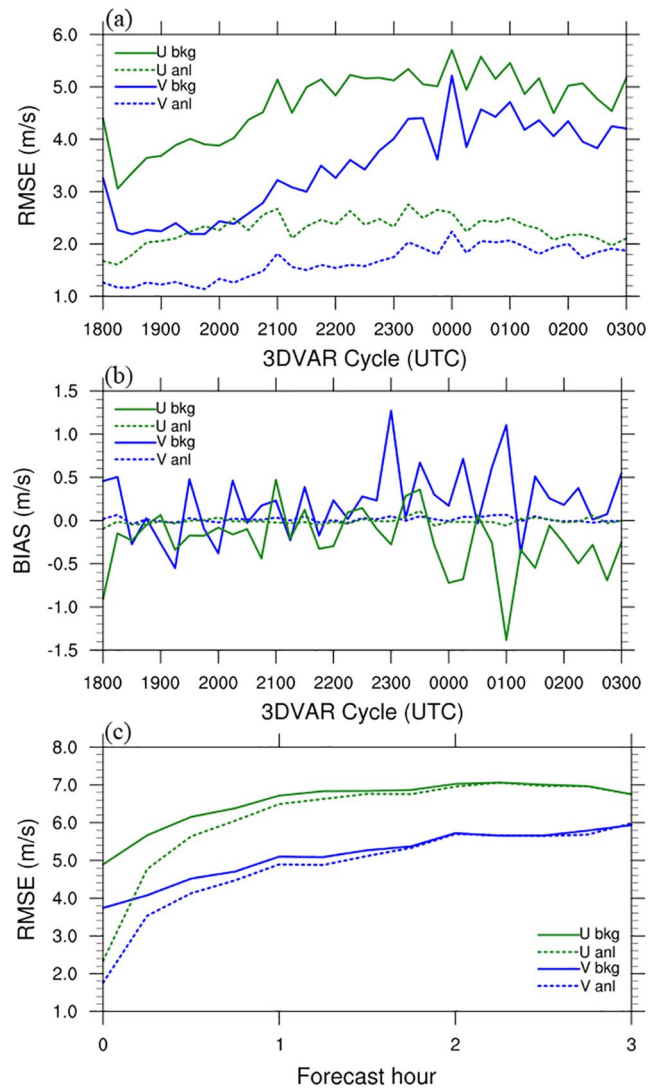
Figure 3. Time series of (a) root-mean-square errors (RMSEs) and (b) biases for u (green), and v (blue) from background (solid) and analysis (dashed) during the assimilation cycles from 1800 to 0300 UTC. (c) Aggregate RMSEs for the nine 3-h free forecasts initialized with the background (solid) and analysis (dashed).

To assess how the AMV DA impacts the mesoscale airflow, the wind analyses and the associated divergence field are examined first (Figure 4). The reason for selecting 2300 UTC May 1, 2018 is that the squall line along the front has been developing into a mature stage until this time and the cumulative benefit from the prior analysis and forecast cycles is also relatively perceptible. The 850-hPa wind and equivalent potential temperature analyses show that the front and dryline boundaries (indicated by the blue thick line in Figure 4a) in NoDA are basically aligned along a line, while the AMV experiment produces a turning point, which is the intersection between a more west-east oriented front and a dryline slightly farther to the western Kansas (Figure 4a vs. Figure 4b). The cyclonic rotation associated with the low over the north Kansas and central Nebraska is slightly enhanced by AMV. And the upper-level divergent flows above the cold pools are more pronounced in AMV than those in NoDA (Figure 4c vs. Figure 4d). It is evident that the pattern of the upper-level divergence field in AMV corresponds better to the area of >30 dBZ observed reflectivity and the corresponding magnitude is also improved by AMV (Figure 4e vs. Figure 4f).

The 1–3 h forecasts of composite reflectivity fields are illustrated in Figure 5 for the NoDA and AMV experiments together with the MRMS observations. The quasi-linear convective system develops along the cold
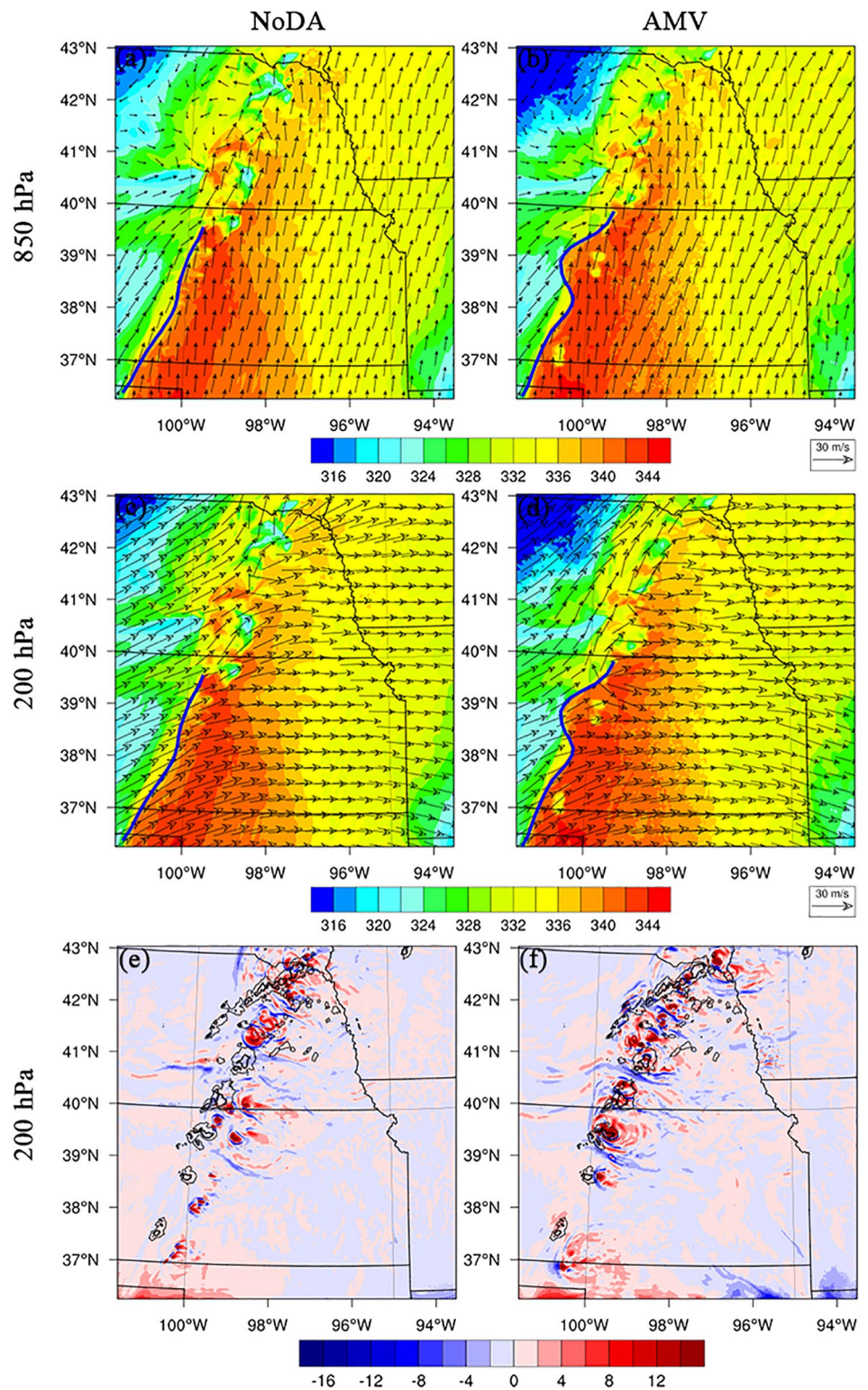
Figure 4. (a) and (b) 850-hPa and (c) and (d) 200-hPa wind analyses (m s^{-1}, vectors) with 850-hPa equivalent potential temperature (k) indicated in colors for (left) NoDA and (right) atmospheric motion vector (AMV) experiments at 2300 UTC May 1, 2018. (e) and (f) 200-hPa divergence analyses (10^{-5} s^{-1}, shaded) for (left) NoDA and (right) AMV experiments. The contours in (e) and (f) represent the MRMS composite reflectivity at 30 and 50 dBZ.
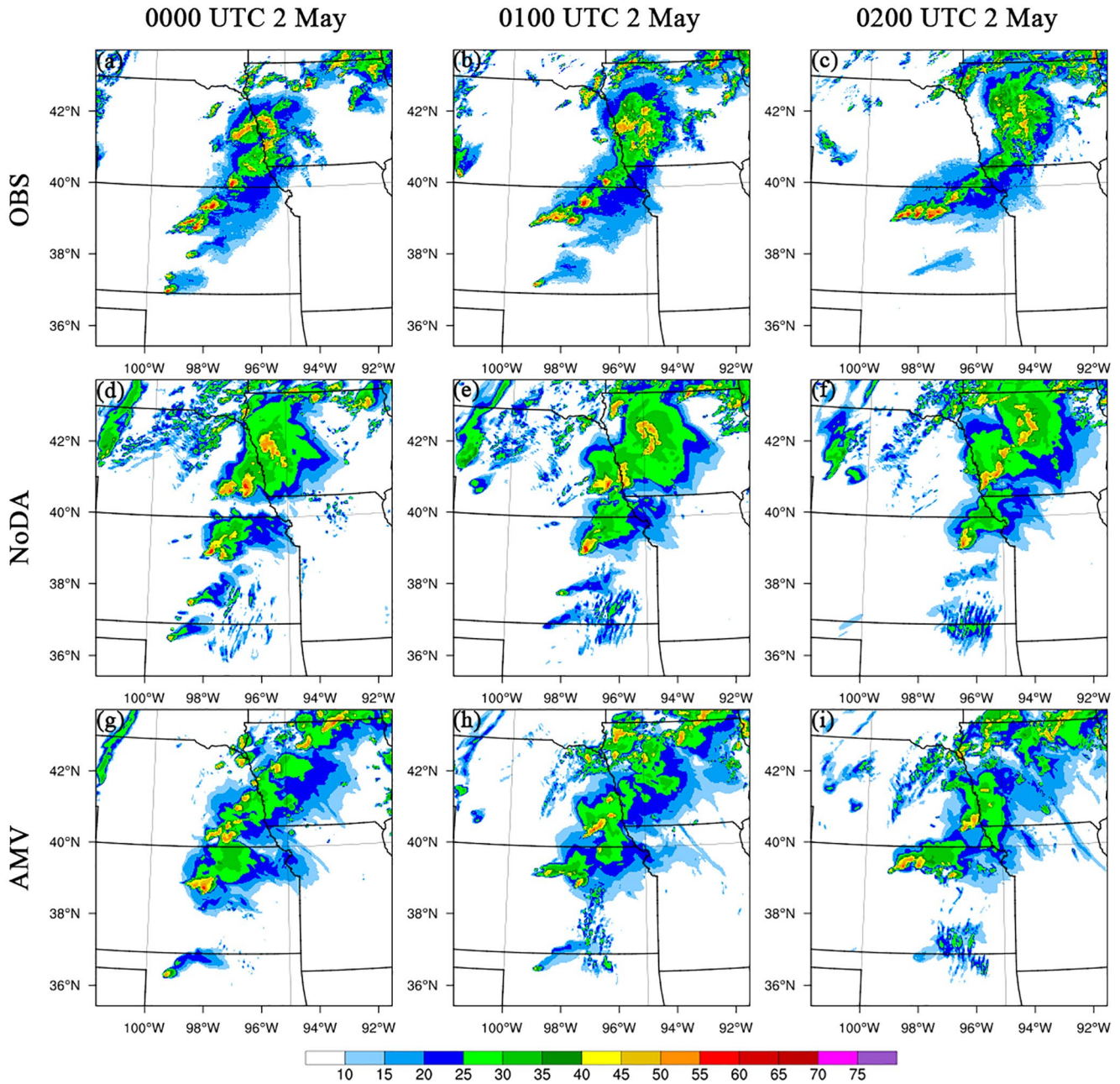
Figure 5. The composite reflectivity (dBZ, shaded) for (a)–(c) MRMS observations interpolated onto the 1.5 km simulation domain, (d)–(f) NoDA, and (g)–(i) AMV experiments at (left, 1-h forecast) 0000 UTC May 2, (middle, 2-h forecast) 0100 UTC May 2, and (right, 3-h forecast) 0200 UTC May 2, 2018.

front as well as the discrete storm cells initiated near the dryline (Figures 5a–5c). NoDA produces two major separated areas of precipitation, more similar to two mesoscale convective systems (MCS), instead of a linear system over northeast Kansas and southwest Iowa (Figures 5d–5f). In contrast, the storms in the AMV experiment show a more linear convective mode, especially for the first hour forecast, and they are comparable to the MRMS observations in terms of shape and location, although individual cells are not perfectly captured (Figures 5g–5i). This indicates that the assimilation of high-resolution AMV data can improve the storm development and movement near the frontal boundary by providing a better representation of storm wind information. However, the discrete cells over the south Kansas are either missed or predicted further southward in the AMV experiment. This occurs because an isolated cell or a smaller cluster of cells may be difficult for the AMV data to discern by nature. Another reason is that only wind data is being assimilated
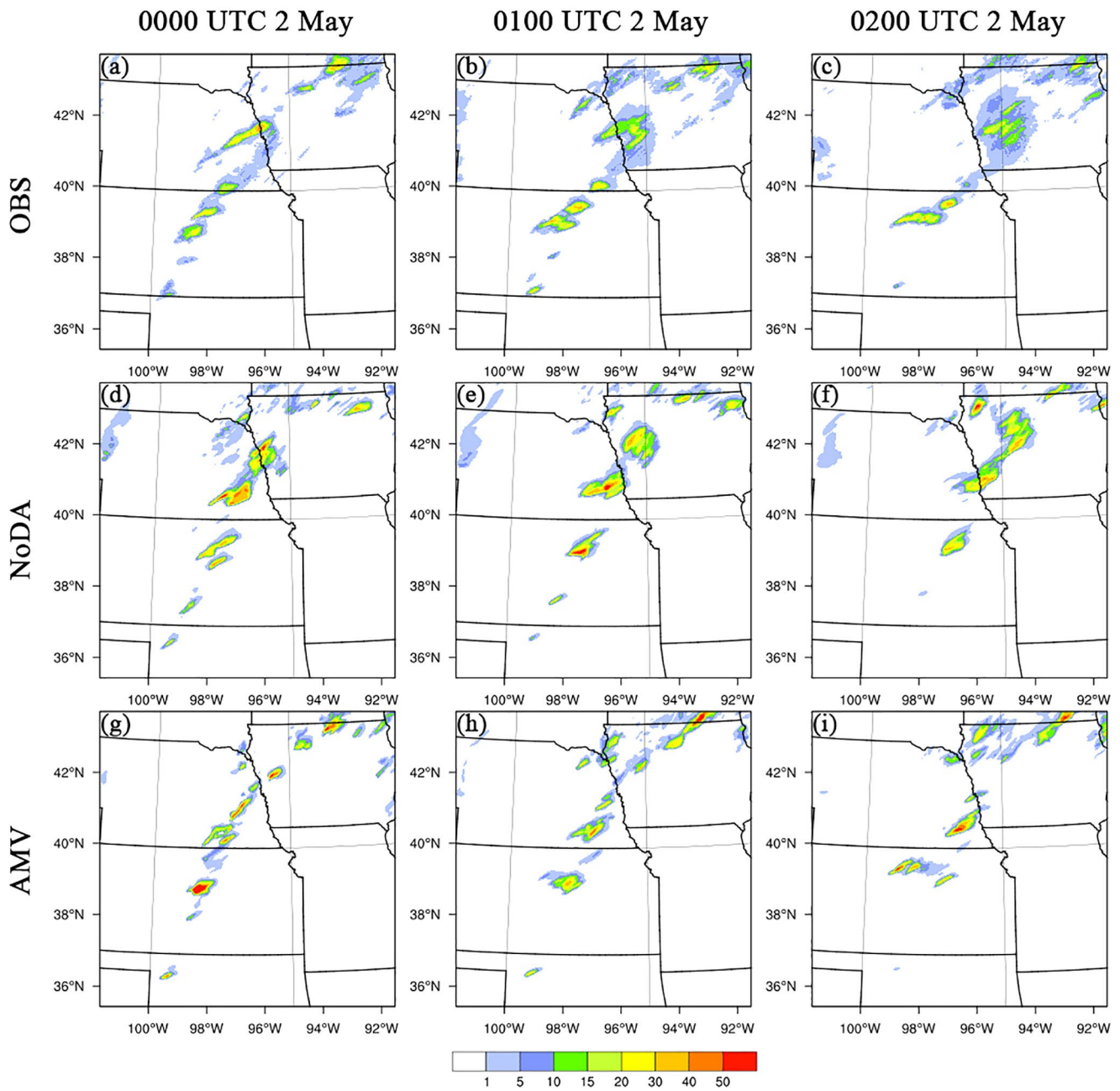
Figure 6. The 1-h accumulated precipitation (APCP) fields (mm, shaded) for (a)–(c) from the Stage IV multi-sensor rainfall estimates, (d)–(f) NoDA, and (g)–(i) AMV experiment at (left, 1-h forecast) 0000 UTC May 2, (middle, 2-h forecast) 0100 UTC May 2, and (right, 3-h forecast) 0200 UTC May 2, 2018.

here, while the timing and location of precipitation are often strongly controlled by the mass field. Furthermore, the hourly accumulated precipitation (APCP) fields from NoDA and AMV are also compared in Figure 6. Along the quasi-linear convective system, the areal coverage of hourly APCP <20 mm is generally improved by the AMV DA. However, both NoDA and AMV appear to mostly overpredict the precipitation amount associated with some cells embedded within the linear system. Specifically, AMV overpredicts the 1-h forecast precipitation over the north Kansas and it underpredicts the rainfall over western Iowa for the 2-h to 3-h forecasts (Figures 6g–6i vs. Figures 6a–6c). This is because a squall line or other mesoscale precipitation features are also difficult to reproduce in a model forecast, as model errors begin growing at small spatiotemporal scales in regions of precipitation, before communicating to the larger-scale flow and transitioning to a slower growth regime (Selz & Craig, 2015).
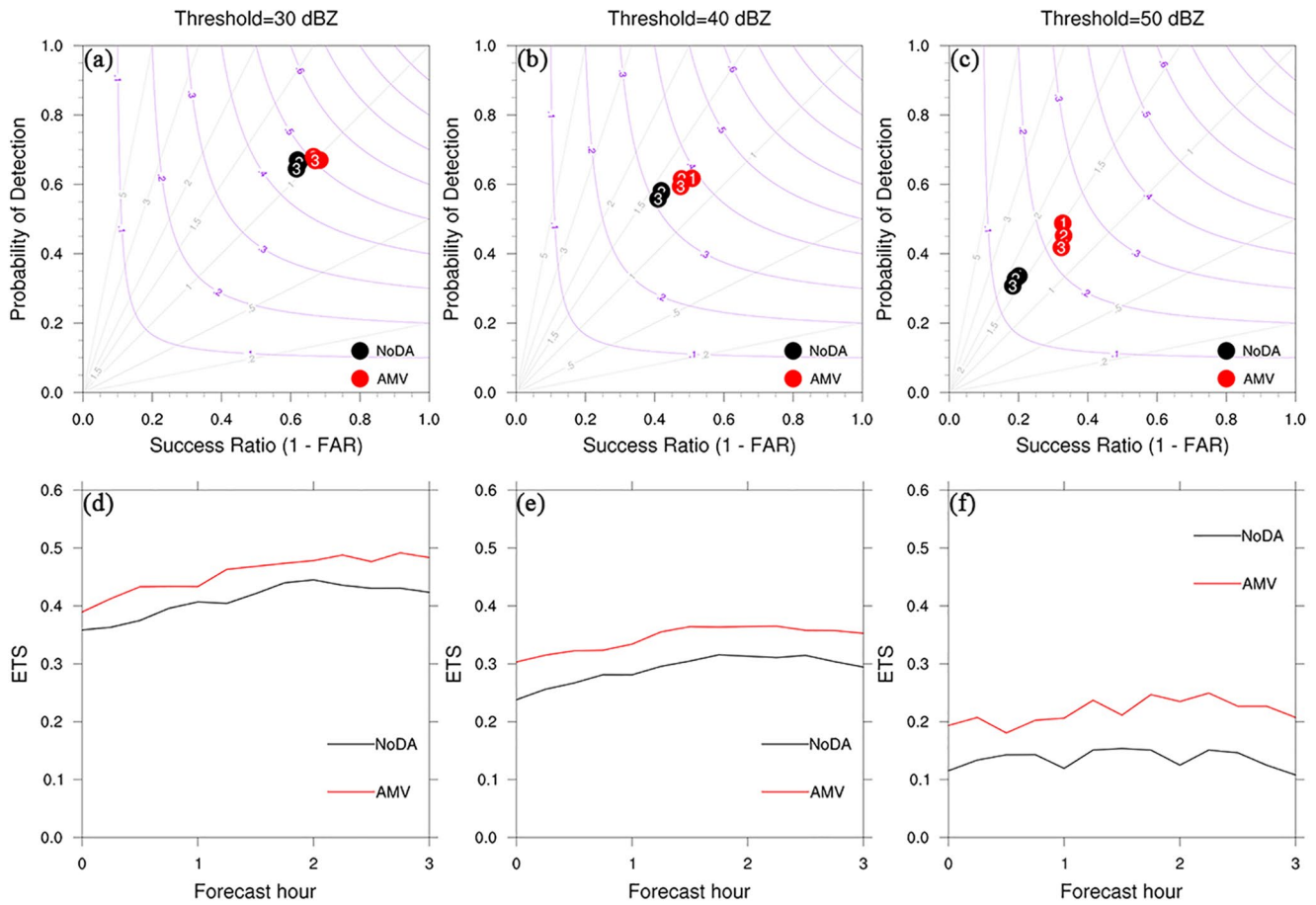
Figure 7. Aggregate score metrics of composite reflectivity fields relative to MRMS observations for nine 3-h free forecasts for the NoDA (black) and AMV (red) experiments in Case 1. (a)–(c) show the performance diagrams at 1-h, 2-h, and 3-h forecast time, and (d)–(f) the equitable threat score (ETS) for (left) 30 dBZ, (middle) 40 dBZ, and (right) 50 dBZ thresholds, respectively. Results are shown for a neighborhood radius of 12-km.

To quantify the performance of the composite reflectivity and APCP forecasts for the AMV DA, the categorical performance diagrams and the neighborhood-based ETS are computed and aggregated over nine 3-h free forecasts launched every hour from 1900 to 0300 UTC. The performance diagram efficiently combines the information derived from key contingency table elements including POD, SR (1—FAR), and CSI (Roebber, 2009). The closer the values of POD, SR, and CSI approach unity, the better forecast is achieved, with the perfect forecast located at the upper-right corner of the diagram. All the score metrics are calculated for a neighborhood radius of 12 km. The ETS for composite reflectivity is computed at 15-min intervals and that for APCP is at hourly intervals. As the composite reflectivity threshold increases from 30 to 50 dBZ, the forecast skill drops dramatically for the NoDA and AMV experiments, owing to decreased PODs along with increased FARs (Figures 7a–7c). Nevertheless, AMV consistently outperforms NoDA at all thresholds for each forecast lead time, with higher POD, SR, CSI, and ETS values. It is also worth noting that the positive impact of AMV DA becomes slightly larger when the reflectivity threshold increases from 30 to 50 dBZ. Similar trends and behavior are obtained in the performance diagrams and ETS figures for the hourly APCP against NCEP Stage IV multisensory rainfall product, highlighting the superior performance of AMV (Figure 8). In terms of the 1-h and 3-h score metrics in the performance diagrams, AMV substantially corrects the significant high bias (black dots closer to the upper-left corner of the diagram) and slightly increases the CSI values, while it generates lower PODs at the same time (Figures 8a–8c). One potential explanation is that the more linear convective mode of APCP forecast with AMV effectively reduces the false alarms with a narrower areal coverage of APCP >20 mm (Figure 6). Combined with the inability of the AMV data to resolve individual cells, lower POD values are obtained.
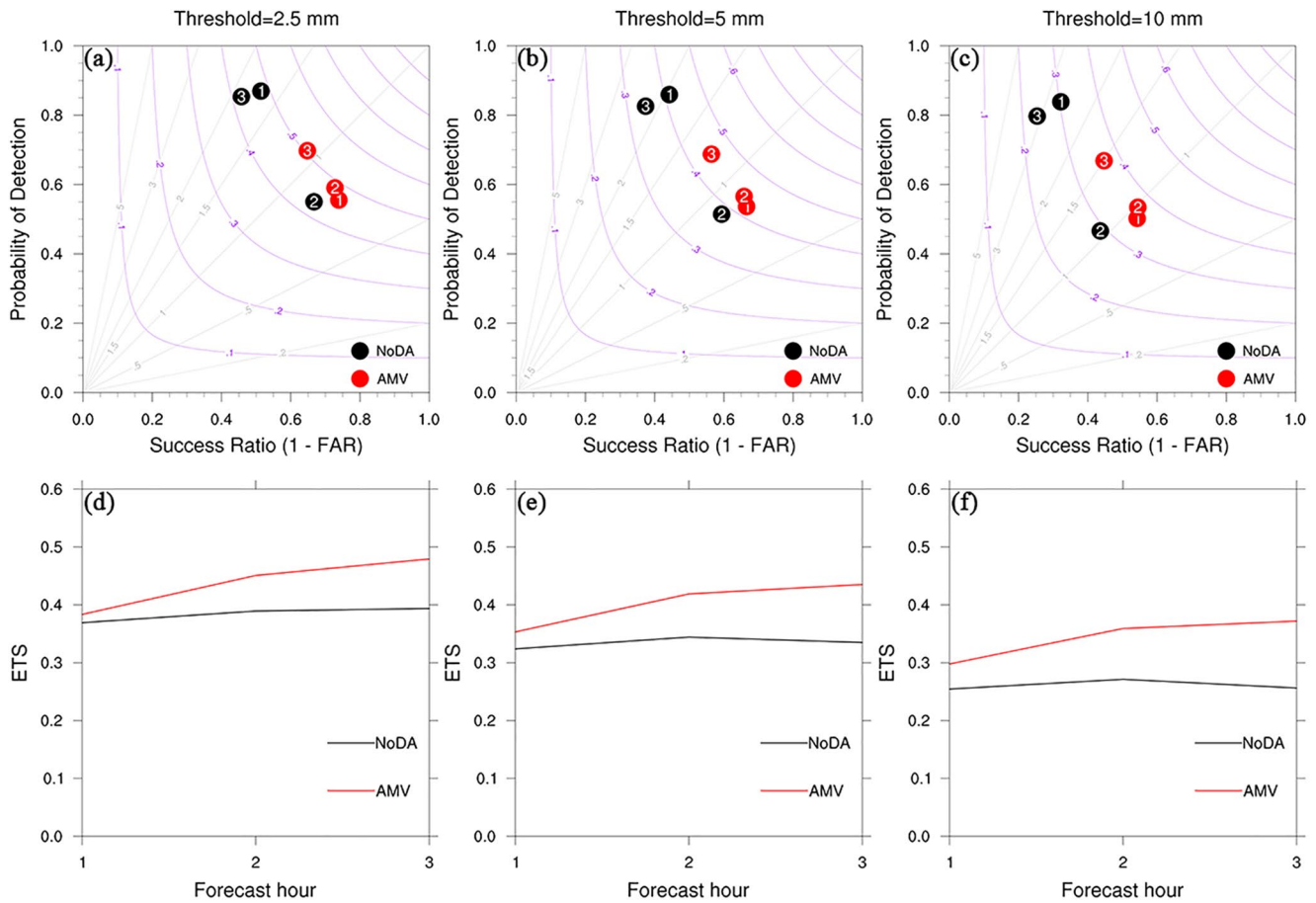
Figure 8. Same as in Figure 7, but for hourly APCP relative to Stage IV rainfall estimates calculated using the following thresholds: (a) and (d) 2.5 mm, (b) and (e) 5 mm, and (c) and (f) 10 mm.

4.2. Case 2: May 28, 2019

On the morning of May 28, 2019, a cluster of elevated thunderstorms initiated in central Kansas, from which the convective outflow reinforced the west-east front across northeast Kansas and northern Missouri. After the elevated convection began to interact with the baroclinic zone in northeast Kansas, it grew upscale by late afternoon into an MCS that spread northeast across northern Missouri and southern Iowa. Meanwhile, a weak surface cyclone in north-central Kansas moved east-northeastward toward Missouri with a trailing cold front shifting slowly southeastward (Figures 11a–11c). To the south of the cyclone, a dryline sharpened across western Oklahoma and northwest Texas. These surface boundaries provided the primary foci for severe thunderstorm development. Between 2300 UTC May 28 and 0200 UTC May 29, a total of 19 tornadoes and several large hail and damaging wind events were reported in Kansas, Missouri, and Oklahoma. An EF-2 tornado was confirmed in Clay County, Missouri around 0100 UTC May 29 by the NWS damage survey team, with a maximum wind of 51.4 m/s and a maximum width of 365 m. Hail up to baseball size (2.75 in.) was reported in Trego County, Kansas and as large as tea cup size (3 inch) in Gove County, Kansas.

In the early 3DVAR cycles for this case, most AMV observations are derived from the visible band within the 1,000–700 hPa layer, by the means of tracking immature, nonprecipitating cumulus (Bedka & Mecikalski, 2005). As the front moved east-northeastward, the associated low-level jet transported the moist and unstable airmass across the warm sector (Figures 9a–9e). During the later cycles (Figures 9f–9i), the AMVs generally represent the flow aloft within the 400–100 hPa layer and most winds are retrieved from the longwave infrared band (11.2 μm). The lack of AMVs in the mid-layer (700–400 hPa) for both cases (Cases
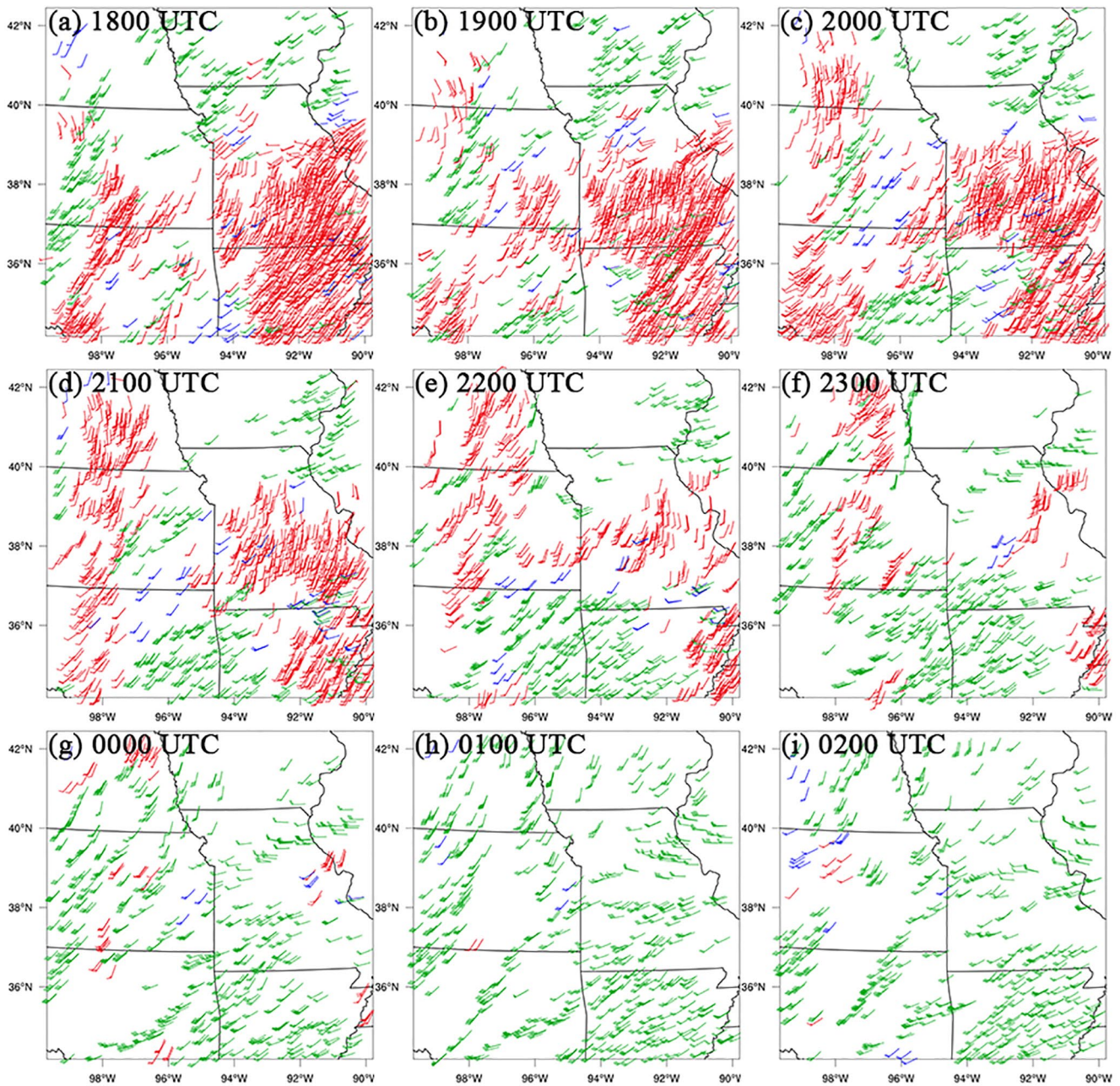
Figure 9. Same as Figure 2, but for the AMV observations from 1800 UTC May 28 to 0200 UTC May 29, 2019 at 1-h intervals.

1 and 2) is due to the nature of the AMV retrieval algorithm. Since the retrieved AMVs show larger errors between 700 and 400 hPa (Sears & Velden, 2012; Velden et al., 2017), the longwave infrared winds within this layer are excluded by the QC procedures.

The analyzed potential temperature and wind fields are examined in Figure 10 as before. For this case, the surface analysis map from Weather Prediction Center (WPC) at 0000 UTC is also shown in Figure 10e. Comparison of Figures 10a and 10b against Figure 10e reveals that the AMV experiment generally captures the west-east front near the Missouri-Iowa state-line, while the front in NoDA extends too far northeastward into central Iowa. It is also noted that the front in the AMV DA experiment is located slightly north to that in the surface analysis map. A possible reason is that there is 1-h time difference between the two figures. Consistent with the 850-hPa temperature and wind analyses, the 200-hPa divergent flows are widely evident
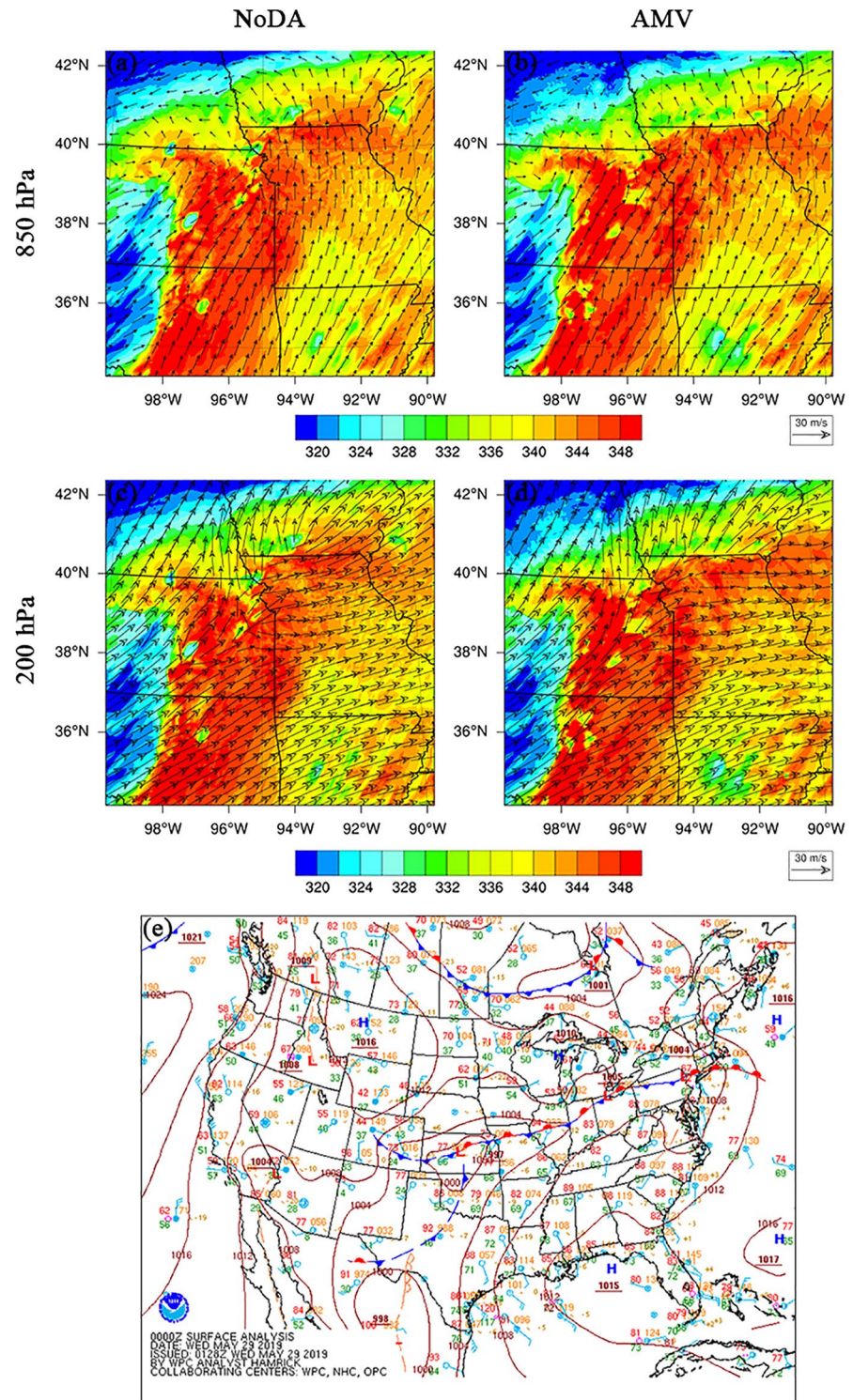
Figure 10. (a)–(b) 850-hPa and (c)–(d) 200-hPa wind analyses (m s⁻¹, vectors) with 850-hPa equivalent potential temperature (k) indicated in colors for (up-middle left) NoDA and (up-middle right) AMV experiments at 2300 UTC May 28, 2019. (e) The Weather Prediction Center (WPC) surface analysis map at 0000 UTC May 29, 2019 (downloaded from https://www.wpc.ncep.noaa.gov/archives/web_pages/sfc/sfc_archive_maps.php?arcdate=05/29/2019&selmap=2019052900&maptype=namussfc).
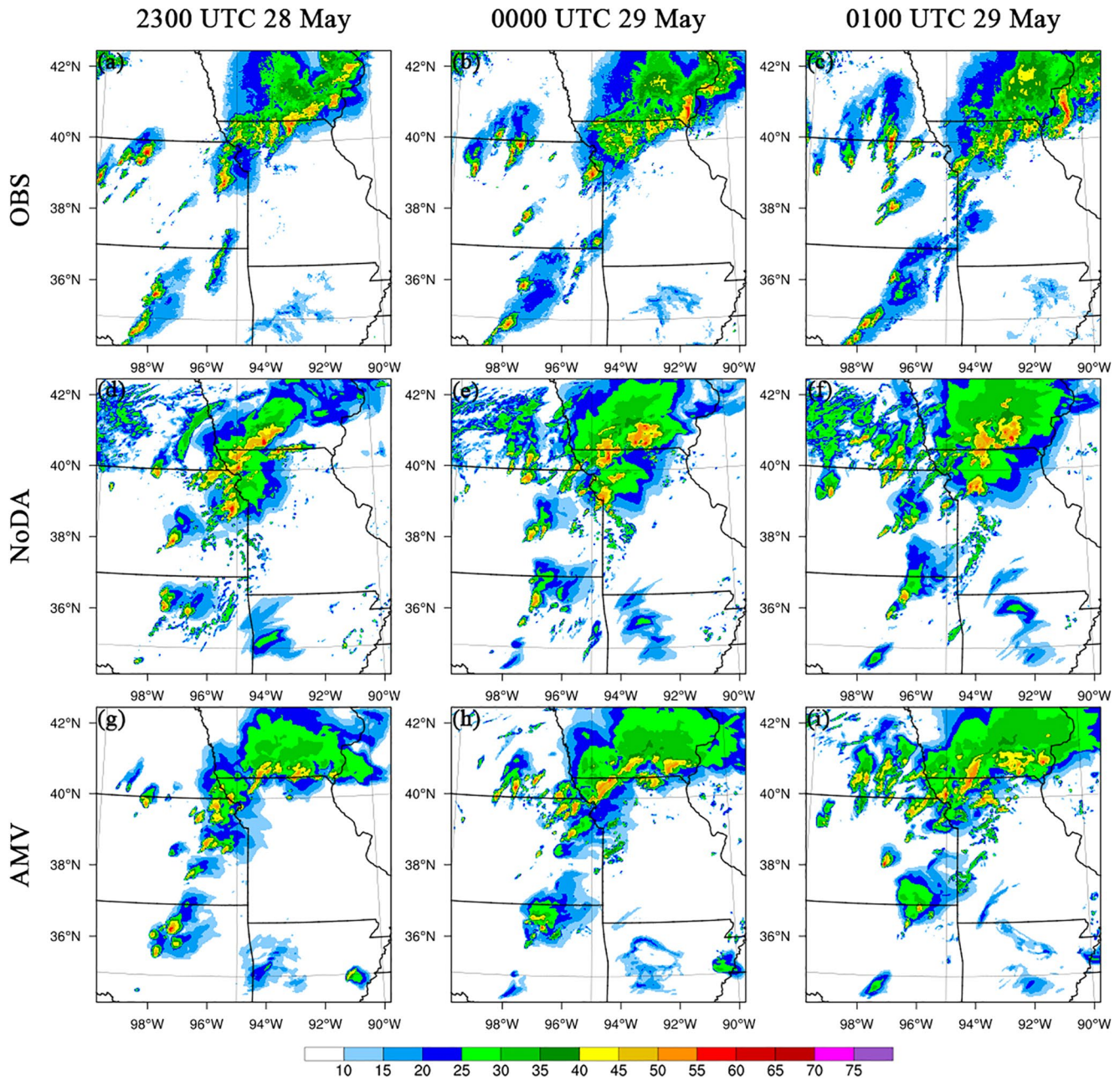
Figure 11. Same as Figure 5, but for (left, analysis time) 2300 UTC May 28, (middle, 1-h forecast) 0000 UTC May 29, and (right, 2-h forecast) 0100 UTC May 29, 2019.

above the cold pools associated with the MCS along the front and the isolated storms over eastern Kansas and northeastern Oklahoma (Figures 10c and 10d).

Owing to a better representation of the thermodynamic environment, AMV reasonably reproduces the MCS across northern Missouri and southern Iowa in terms of location and intensity, correcting the notable slower and northward propagation bias in the NoDA storm forecast (Figure 11). As is seen, both NoDA and AMV underpredict the widely scattered storms farther south along the dryline. This occurs because AMV DA does not help reduce the analysis errors for the variables not directly related to wind observations, such as humidity, which is also indicated by the idealized experiments in Part I of this study. Therefore, similar to NoDA, the AMV experiment still underestimates the sharp humidity gradient along the dryline (not shown). Consistent with the reflectivity forecasts, AMV improves the areal coverage of
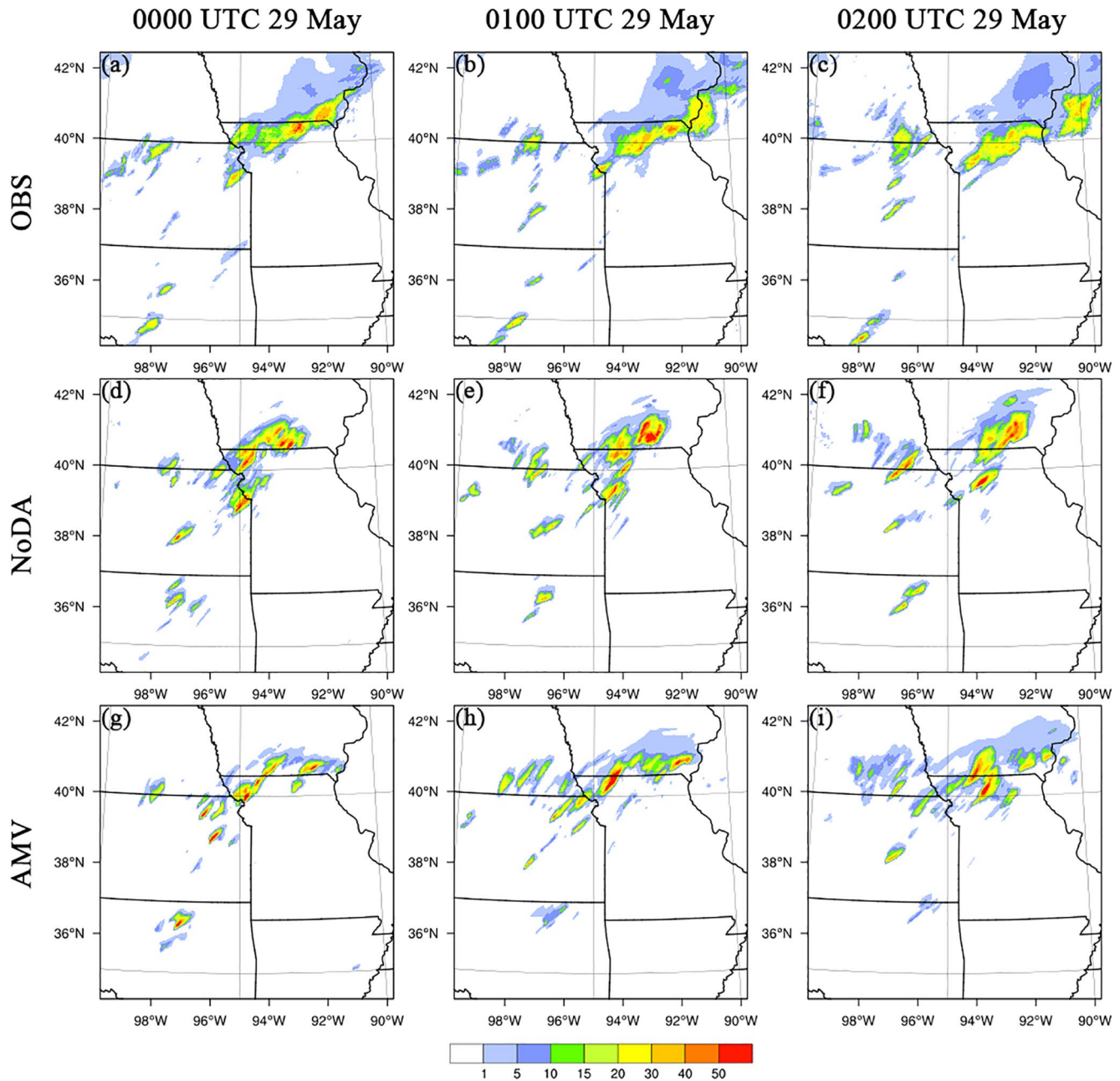
Figure 12. Same as Figure 6, but for (left, 1-h forecast) 0000 UTC May 29, (middle, 2-h forecast) 0100 UTC May 29, and (right, 3-h forecast) 0200 UTC May 29, 2019.

1–3 h APCP forecasts across the Missouri-Iowa border with somewhat larger or smaller rainfall amounts compared to observations, especially for general better rainfall position and cell alignment in the first 2 h (Figure 12).

From the aggregate forecast statistics for composite reflectivity, the improvements of ETS and CSI by AMV over NoDA persist through the 1–3 h forecasts, although the difference between them decreases for later forecasts (Figure 13). For the 30-dBZ and 40-dBZ thresholds, the higher forecast skill produced by AMV is largely due to an increased POD, with SR being approximately constant or slightly smaller (Figures 13a and 13b). At 50 dBZ, however, AMV produces higher POD and SR, which is more notable
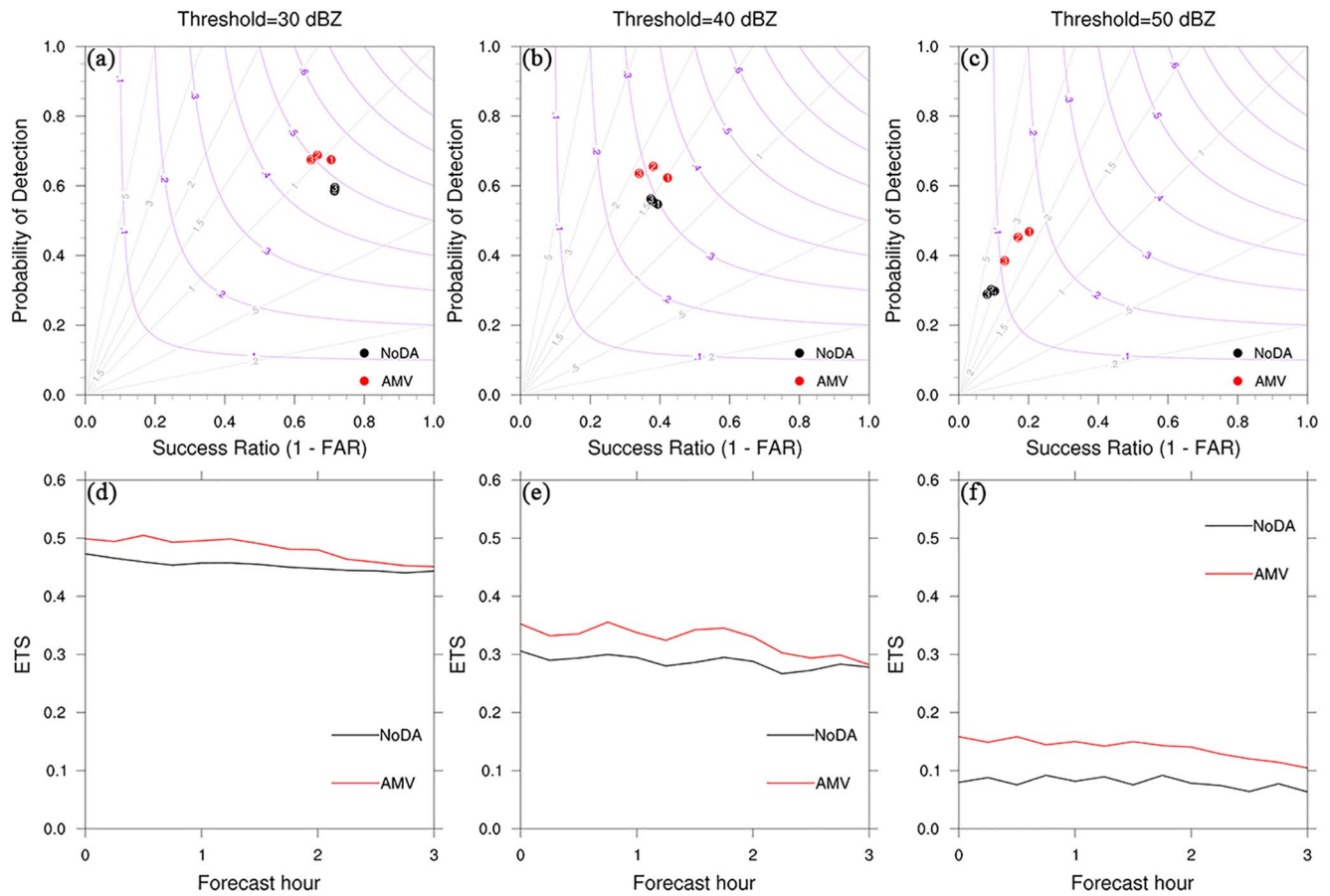
Figure 13. Same as Figure 7, but for case 2.

during the first 2 h (Figure 13c). In terms of APCP, AMV tends to show overall larger values of SR and CSI but smaller PODs (Figures 14a–14c). For all APCP thresholds, AMV persistently produces larger ETS at 3-h forecasts although being small (e.g., <0.3 at 10 mm) and not significantly outperforming NoDA (Figures 14d–14f).

4.3. Case 3: May 17, 2019

Through May 17, 2019 afternoon and evening, an intensifying High Plains surface low moved northeastward out of Colorado across Nebraska, along with an eastward shifting upper-level trough. This contributed to a pronounced jet streak in the low- and mid-troposphere and favorable deep-layer shear for organized storms across western-central Nebraska, where multiple tornadoes and hail events were reported. A warm front extended eastward from the surface low, and transitioned into a cold front across the Ohio Valley/mid-Atlantic. In addition, a dryline was present across western Kansas where several storms developed causing several tornadoes and very large hail owing to the favorable large-scale environment.

Figure 15 highlights how the AMV DA benefits the storm wind environment as well as the thermodynamic analyses through the successive model adjustments to the background fields from the prior analysis cycles. NoDA underestimates the sharp temperature gradient associated with the front boundary across northwestern Nebraska (indicated by the blue thick line in Figure 15b) while the AMV experiment successfully captures it with stronger low-level warm advection and cold surge on the west side of the front. Discrete storms developed near the surface low at the intersection of the front and dryline and eventually organized into a linear mode spreading northeast through the destabilizing warm sector (Figures 16a–16c). Comparison of Figures 16d–16f against Figures 16a–16c reveals
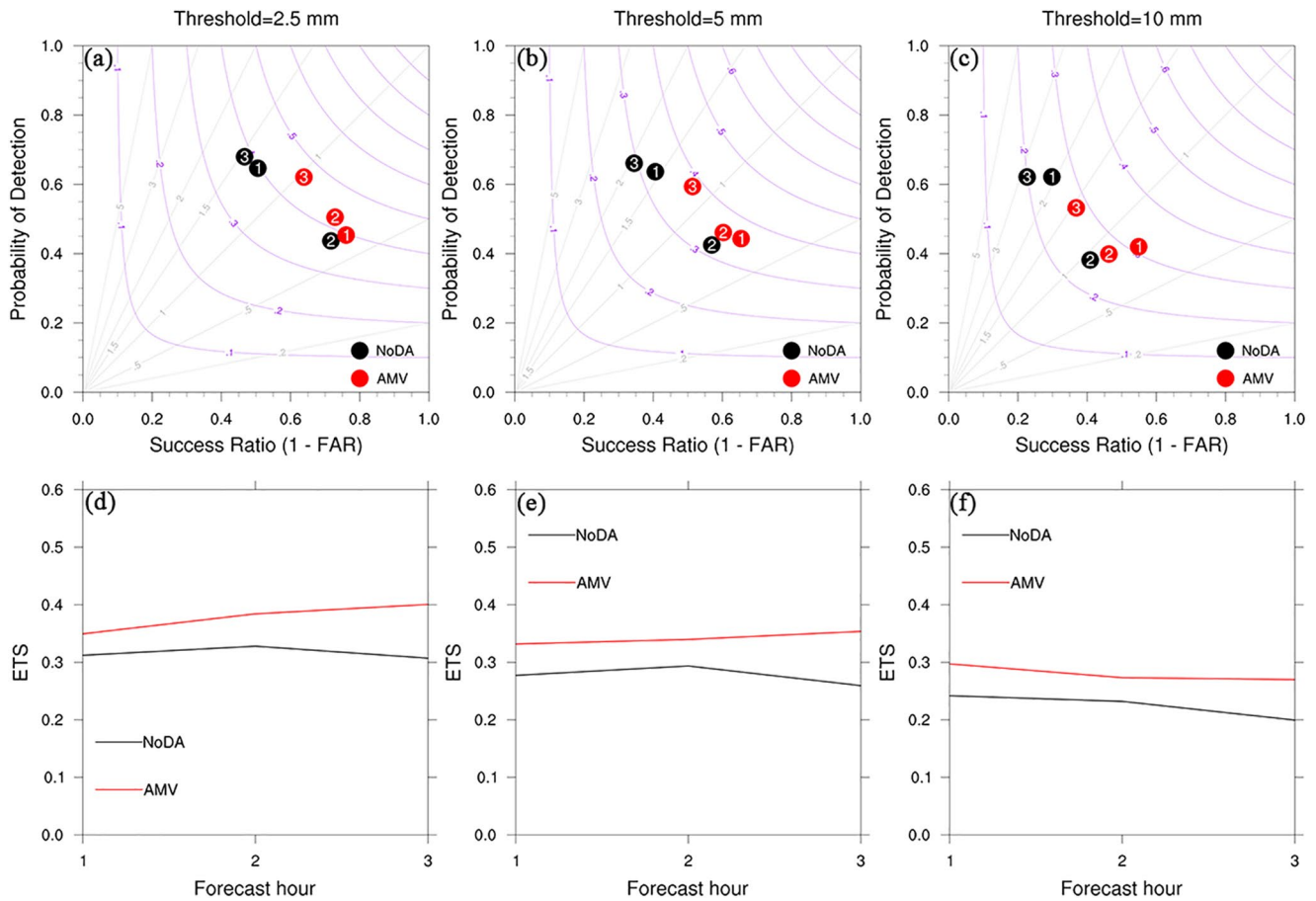
Figure 14. Same as Figure 8, but for case 2.

that a faster and eastward movement bias is present over Nebraska in the NoDA storm forecasts. Owing to the more favorable storm environment (Figure 15b), the AMV experiment yields approximately comparable quasi-linear deep convection evolving across western Nebraska with slightly weaker bias (Figures 16g–16i). However, light spurious stratiform precipitation widely occurred across eastern Nebraska and Kansas in the 3-h forecast (Figure 16i). It is also seen that both AMV and NoDA fail to simulate the isolated cells initiated farther south along the dryline across western Kansas. This is because neither experiment reproduces such a sharp humidity gradient in this region, with the moisture gradient in AMV even slightly weaker (Figures 15c and 15d). The humidity gradient is crucial to the dryline, which is defined simply as a sharp boundary between moist air and dry air. As expected, the AMV experiment generally improves the areal coverage of 1–3 h APCP forecasts across west-central Nebraska, in spite of the bias in the rainfall amount (Figure 17). However, it misses the precipitation associated with the dryline in western Kansas.

Similar to the results discussed in previous cases, aggregate forecast statistics for nine separate 3-h forecasts are computed to provide a more comprehensive view of the AMV DA impact. For the 1–3 h reflectivity forecasts, AMV shows an overwhelming superiority over NoDA with much higher POD, CSI, SR, and ETS at all the thresholds (Figure 18). The weaker bias in reflectivity forecasts (Figure 16) results in overall small values of POD and ETS at 50 dBZ (Figures 18c and 18f). In terms of APCP, AMV exhibits notably less false alarms and larger CSI but smaller POD values at 1-h and 3-h forecasts (Figures 19a–19c). For all the three thresholds, the improvement of ETS by AMV over NoDA persists through the 1–3 h forecasts (Figures 19d–19f).
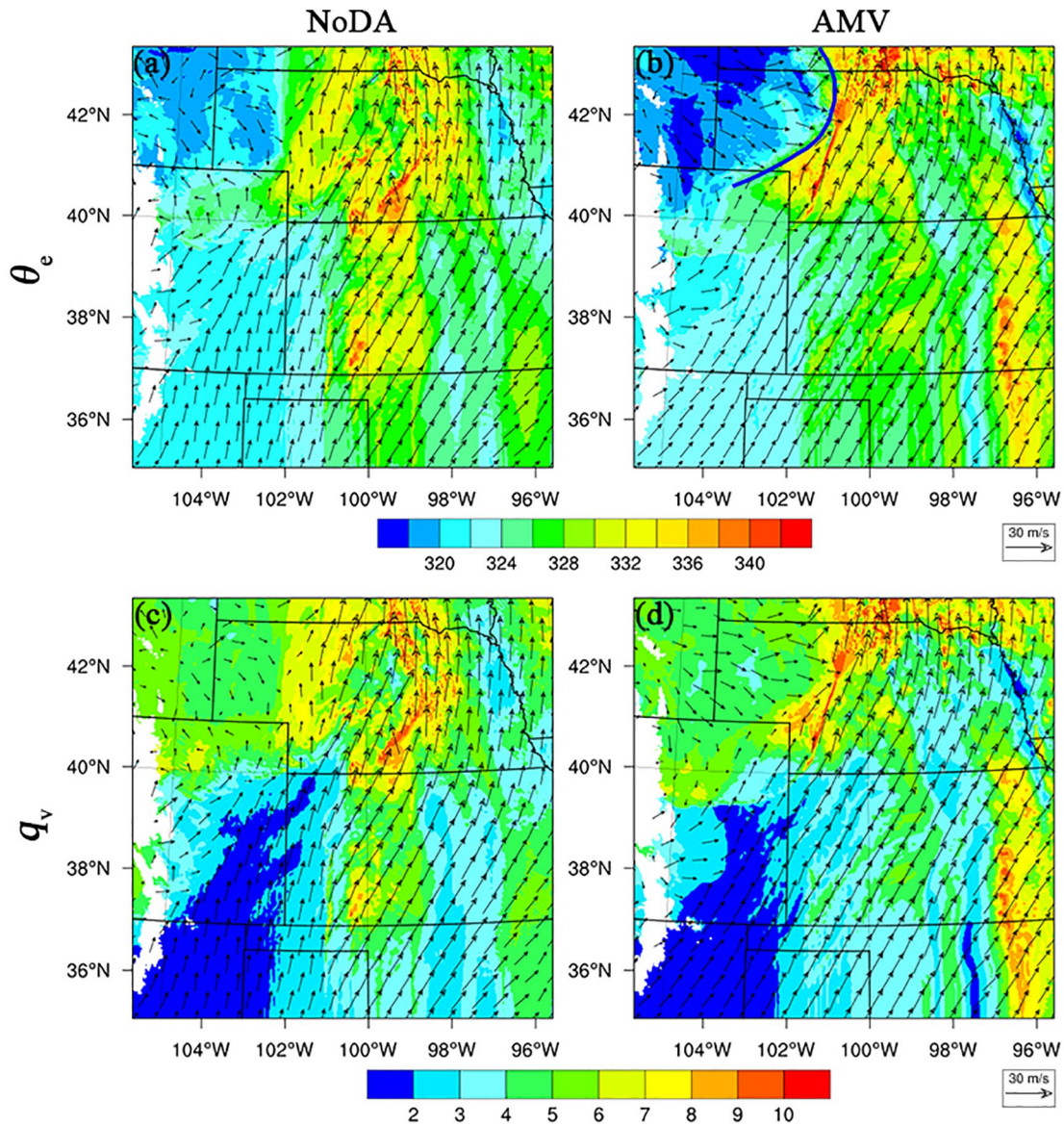
Figure 15. 700-hPa wind analyses (m s^{-1}, vectors) with (a)–(b) equivalent potential temperature (K), and (c)–(d) water vapor mixing ratio (g kg^{-1}) indicated in colors for (left) NoDA and (right) AMV experiments at 0100 UTC May 18, 2019.

5. Summary and Conclusions

This study investigates the impact of assimilating GOES-16 derived AMV observations using the NSSL 3DVAR system and WRF model on the short-term severe weather forecasts. The assessment of the AMV DA performance is carried out with three high-impact weather events that occurred in spring 2018 and 2019 over the Great Plains of the United States. First, the lower-level and upper-level wind analyses and the associated divergence field and potential temperature fields are examined for each case. Then the short-term forecasts of composite reflectivity and hourly APCP are quantitatively verified against the MRMS and Stage IV products in the form of performance diagrams and ETS values.

The vertical distribution of the AMV observations available for assimilation in each case varies with the derivation channels used to track cloud or clear-sky water vapor under different atmospheric conditions. The
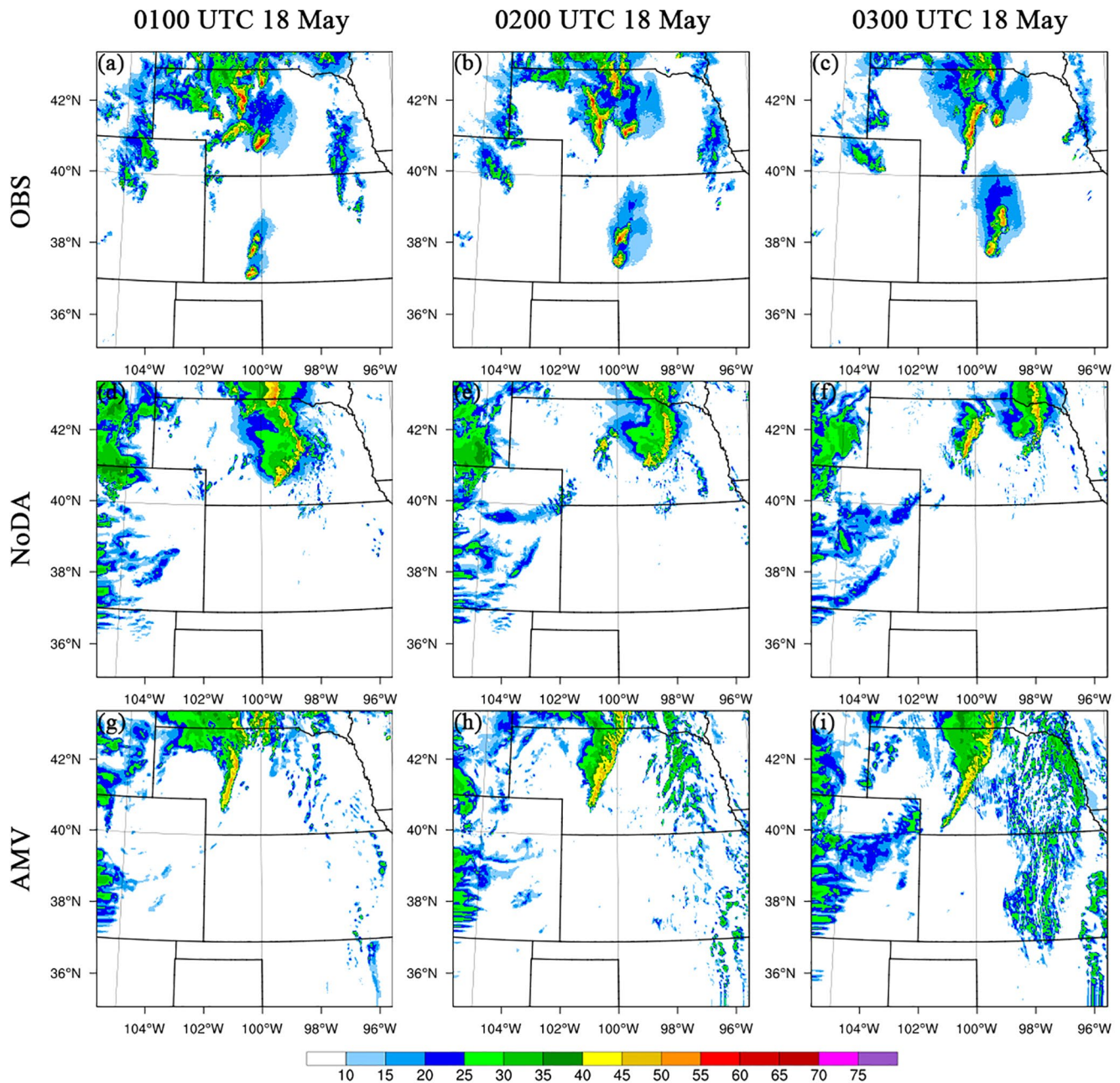
Figure 16. Same as Figure 5, but for (left, analysis time) 0100 UTC May 18, (middle, 1-h forecast) 0200 UTC May 18, and (right, 2-h forecast) 0300 UTC May 18, 2019.

results from the three convective events exhibit a bimodal pattern with maximum AMV number in the upper (400–100 hPa) and lower (1,000–700 hPa) troposphere, which is similar to many earlier AMV DA studies. The lack of AMVs in the mid-layer (700–400 hPa) is determined by the nature of the retrieval algorithm.

The wind analyses for the large-scale environment and mesoscale convective systems are improved by the assimilation of GOES-16 AMVs. The upper-level divergence associated with the deep convection is also enhanced. Moreover, the AMV DA benefits the equivalent potential temperature fields through the successive adjustments during the model integration from the prior 3DVAR analysis cycles. These improvements lead to better simulation of the location and shape for the boundaries including fronts and cyclones, that influences the subsequent storm evolution and movement. For the quasi-linear or MCS along the boundaries, the AMV
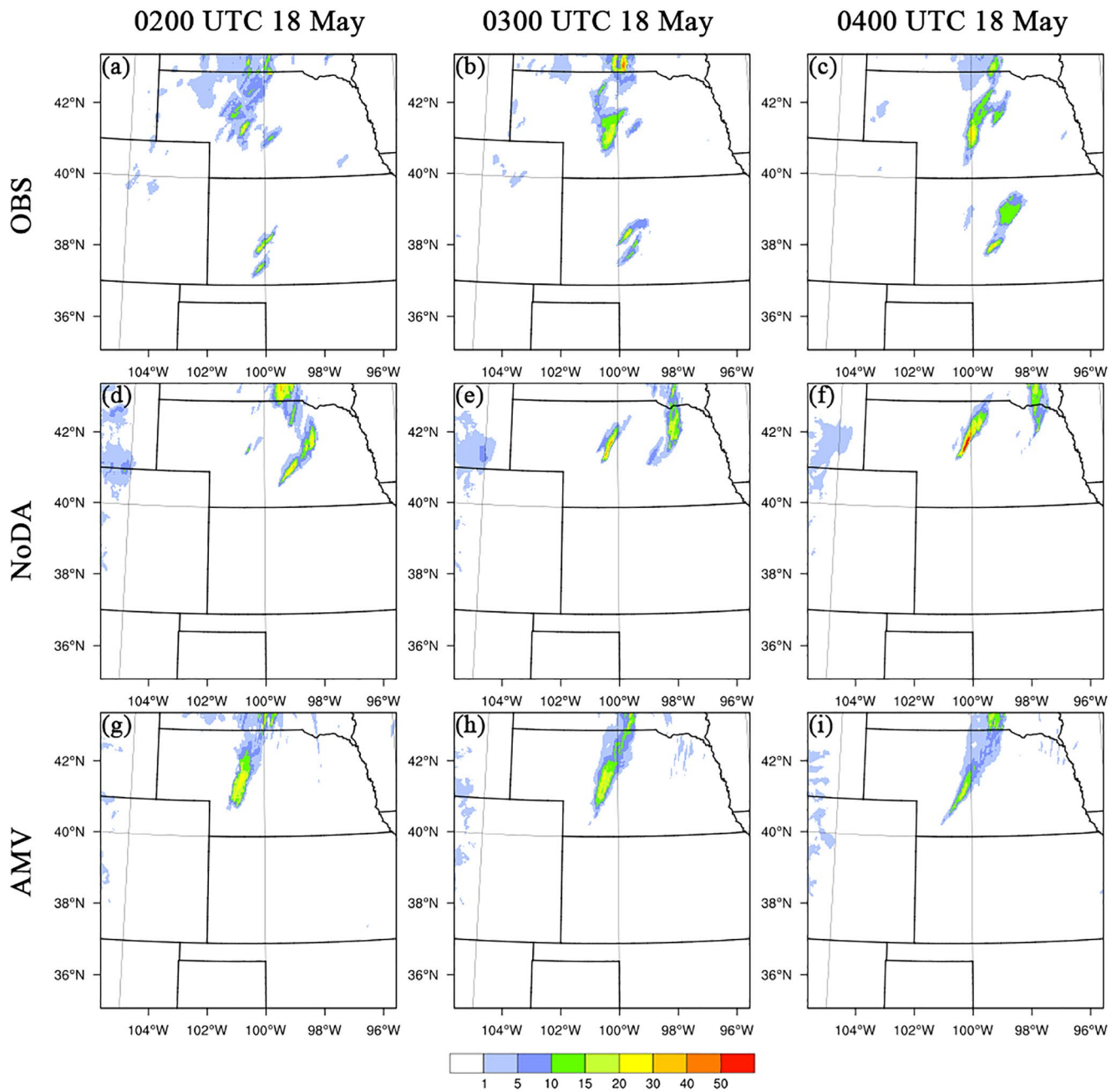
Figure 17. Same as Figure 6, but for (left, 1-h forecast) 0200 UTC May 18, (middle, 2-h forecast) 0300 UTC May 18, and (right, 3-h forecast) 0400 UTC May 18, 2019.

DA outperforms NoDA by yielding more reasonable short-term (0–3 h) forecasts of composite reflectivity and accumulated precipitation in terms of their shape, location, and magnitude. Overall, the aggregate forecast statistics indicate the positive impact of AMV DA on reflectivity and APCP forecasts, although the trends of POD and SR forecasts seem to be case-dependent. However, the AMV DA has difficulty in capturing the sharp moisture gradient associated with the dryline and generally underpredicts the associated scattered storms. This is because AMV DA has difficulty in reducing the analysis errors for the variables not directly related to wind observations, such as humidity. Given the spatial resolution of the current GOES-16 AMV product, the isolated cells or quite small clusters of cells may not be discernable by the AMV data.
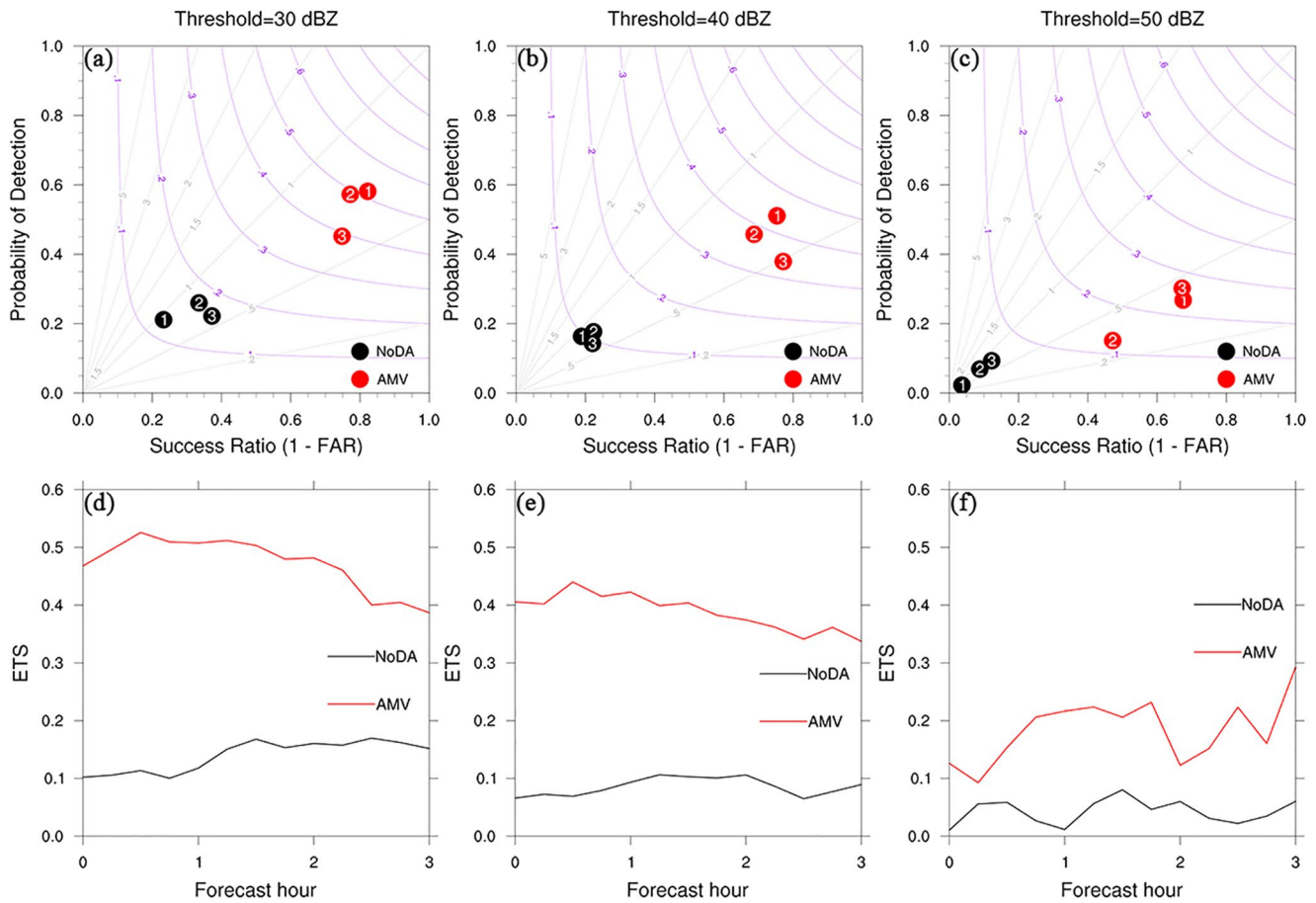
Figure 18. Same as Figure 7, but case 3.

Although this study shows the usefulness of the high-resolution GOES-16 AMV data for improving convective scale short-term forecasts, more issues related to the AMV DA should be addressed in future. Due to the complexity in estimating AMVs errors, further research will be devoted to refining the observation error estimation, including the consideration of error variations with height and/or satellite band. The application of the AMV DA to different phases in a life cycle of a convective storm will also be tested. For example, the AMVs before the cumulus stage could be separately assimilated to assess its impact on convection initiation in the unstable atmosphere. This two-part study, which compares experiments with and without AMV DA, is intended to be representative of the maximum possible amount of new information that can be added when assimilating AMVs for the desired purpose. It is possible that assimilating radar radial velocity data combined with AMV DA can make up for their respective observation gaps. So as a next step, the impact of assimilating both radar and AMV data on the convective scale NWP, especially for the storm structure forecast and isolated cell initiation, will be investigated in the near future. The added value of AMV data will also be investigated within the NSSL3DVAR system in which all available observations are used currently.

Although the deficiency in the static background errors of 3DVAR is partially compensated by performing highly frequent DA cycling, it is likely that better AMV DA results can be achieved by using flow-dependent background error covariance. For example, ensemble-based prior errors may provide a more dynamically consistent link between upper-level winds and low-level moisture during the DA process. Therefore, assimilation of the GOES-16 derived AMVs by using an En3DVar system (Gao et al., 2016), which uses the flow-dependent covariance derived from an ensemble of forecasts, will be investigated in the near future and presented in the third part of this study.
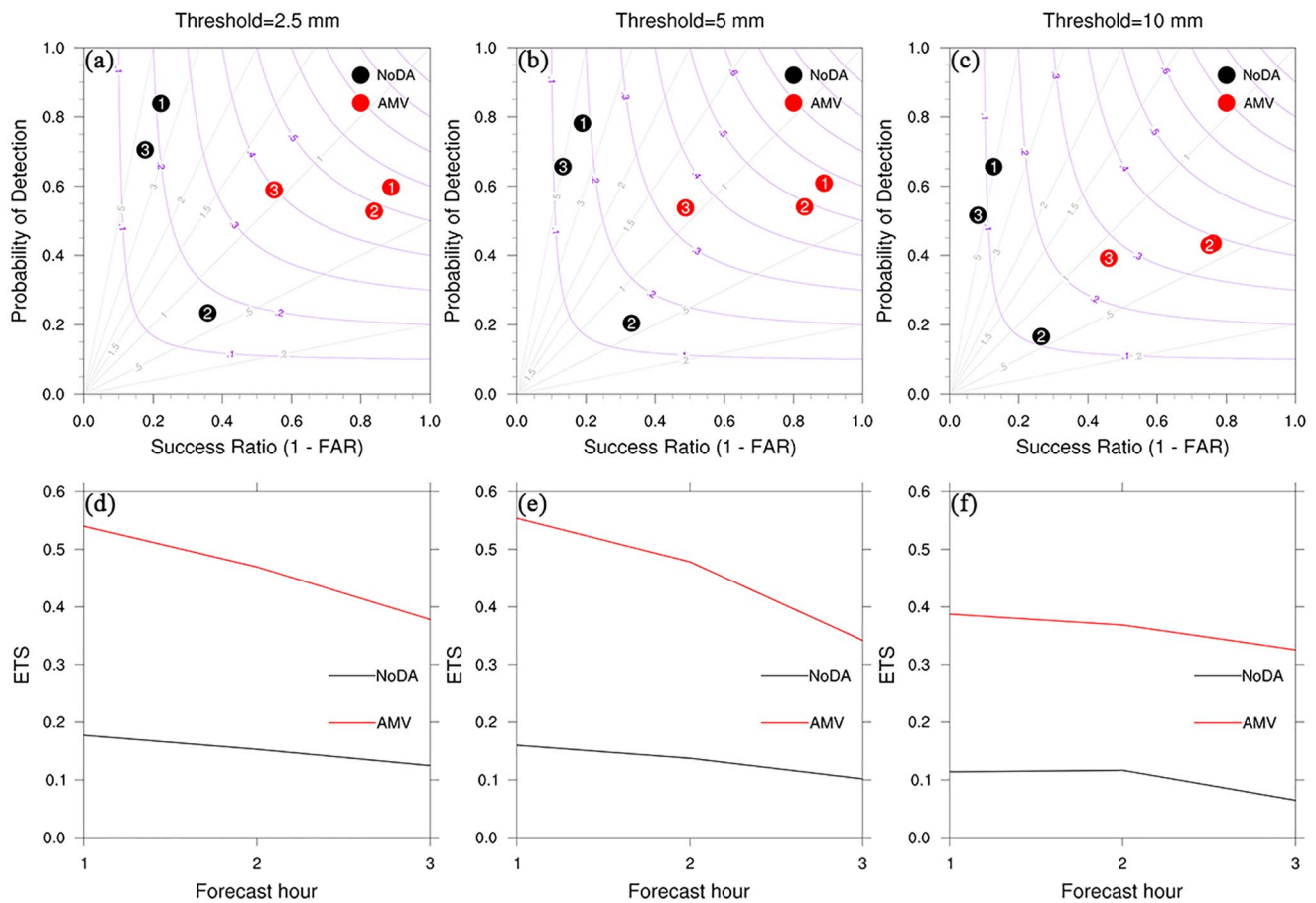
Figure 19. Same as in Figure 8, but for case 3.

Data Availability Statement

The source codes of WRF model version 3.6.1 could be downloaded after filling in the E-mail address (https://www2.mmm.ucar.edu/wrf/users/download/get_source.html). The GOES-16 ABI Level 2 (L2) AMV data were obtained online (https://www.bou.class.noaa.gov/saa/products/search?sub_id=0&datatype_family=GRABIPRD&submit.x=15&submit.y=6). The Multi-Radar Multi-Sensor (MRMS) and the Stage IV rainfall products, and the aggregate forecast statistics for composite reflectivity and APCP are accessible online (https://doi.org/10.5281/zenodo.4495919).

References

Baldwin, M. E., & Mitchell, K. E. (1997). *The NCEP hourly multisensor U.S. precipitation analysis for operations and GCIP research*. Presented at the Preprints, 13th Conference on Hydrology (pp. 54–55). Long Beach, CA: American Meteorological Society.

Bedka, K. M., & Mecikalski, J. R. (2005). Application of satellite-derived atmospheric motion vectors for estimating mesoscale flows. *Journal of Applied Meteorology*, *44*(11), 1761–1772. https://doi.org/10.1175/JAM2264.1

Benjamin, S. G., Grell, G. A., Brown, J. M., Smirnova, T. G., & Bleck, R. (2004). Mesoscale weather prediction with the RUC hybrid isentropic–terrain-following coordinate model. *Monthly Weather Review*, *132*(2), 473–494. https://doi.org/10.1175/1520-0493(2004)132<0473:MWPWTR>2.0.CO;2

Cherubini, T., Businger, S., Velden, C., & Ogasawara, R. (2006). The impact of satellite-derived atmospheric motion vectors on mesoscale forecasts over Hawaii. *Monthly Weather Review*, *134*(7), 2009–2020. https://doi.org/10.1175/MWR3163.1

Clark, A. J., Gallus, W. A., & Weisman, M. L. (2010). Neighborhood-based verification of precipitation forecasts from convection-allowing NCAR WRF model simulations and the operational NAM. *Weather and Forecasting*, *25*(5), 1495–1509. https://doi.org/10.1175/2010WAF2222404.1

Daniels, J., Bresky, W., Wanzong, S., Velden, C., & Berger, H. (2012). *GOES-R advanced baseline imager (ABI) algorithm theoretical basis document for derived motion winds* (No. Version 2.5). Retrieved from https://www.star.nesdis.noaa.gov/goesr/docs/ATBD/DMW.pdf

Doswell, C. A. (Ed.), (2001). *Severe convective storms*. Boston, MA: American Meteorological Society. https://doi.org/10.1007/978-1-935704-06-5

Dudhia, J. (1989). Numerical study of convection observed during the winter monsoon experiment using a mesoscale two-dimensional model. *Journal of the Atmospheric Sciences*, *46*(20), 3077–3107. https://doi.org/10.1175/1520-0469(1989)046<3077:NSOCOD>2.0.CO;2

Elsberry, R. L., Hendricks, E. A., Velden, C. S., Bell, M. M., Peng, M., Casas, E., & Zhao, Q. (2018). Demonstration with special TCI-15 datasets of potential impacts of new-generation satellite atmospheric motion vectors on navy regional and global models. *Weather and Forecasting*, *33*(6), 1617–1637. https://doi.org/10.1175/WAF-D-17-0168.1

Fierro, A. O., Wang, Y., Gao, J., & Mansell, E. R. (2019). Variational assimilation of radar data and GLM lightning-derived water vapor for the short-term forecasts of high-impact convective events. *Monthly Weather Review*, *147*(11), 4045–4069. https://doi.org/10.1175/MWR-D-18-0421.1

Gao, J., Fu, C., Stensrud, D. J., & Kain, J. S. (2016). OSSEs for an ensemble 3DVAR data assimilation system with radar observations of convective storms. *Journal of the Atmospheric Sciences*, *73*(6), 2403–2426. https://doi.org/10.1175/JAS-D-15-0311.1

Gao, J., Smith, T. M., Stensrud, D. J., Fu, C., Calhoun, K., Manross, K. L., et al. (2013). A real-time weather-adaptive 3DVAR analysis system for severe weather detections and warnings. *Weather and Forecasting*, *28*(3), 727–745. https://doi.org/10.1175/WAF-D-12-00093.1

Gao, J., & Stensrud, D. J. (2012). Assimilation of reflectivity data in a convective-scale, cycled 3DVAR framework with hydrometeor classification. *Journal of the Atmospheric Sciences*, *69*(3), 1054–1065. https://doi.org/10.1175/JAS-D-11-0162.1

Gao, J., & Stensrud, D. J. (2014). Some observing system simulation experiments with a hybrid 3DEnVAR system for storm-scale radar data assimilation. *Monthly Weather Review*, *142*(9), 3326–3346. https://doi.org/10.1175/MWR-D-14-00025.1

Gao, J., Xue, M., Brewster, K., & Droegemeier, K. K. (2004). A three-dimensional variational data analysis method with recursive filter for Doppler radars. *Journal of Atmospheric and Oceanic Technology*, *21*(3), 457–469. https://doi.org/10.1175/1520-0426(2004)021<0457:ATVDAM>2.0.CO;2

Goerss, J. S., Velden, C. S., & Hawkins, J. D. (1998). The impact of multispectral GOES-8 wind information on Atlantic tropical cyclone track forecasts in 1995. Part II: NOGAPS forecasts. *Monthly Weather Review*, *126*(5), 1219–1227. https://doi.org/10.1175/1520-0493(1998)126<1219:TIOMGW>2.0.CO;2

Goodman, S. J., Gurka, J., DeMaria, M., Schmit, T. J., Mostek, A., Jedlovec, G., et al. (2012). The GOES-R proving ground: Accelerating user readiness for the Next-Generation Geostationary Environmental Satellite System. *Bulletin of the American Meteorological Society*, *93*(7), 1029–1040. https://doi.org/10.1175/BAMS-D-11-00175.1

Hamada, T. (1983). On the optimal time-interval of satellite image acquisition for operational cloud motion wind derivation (Vol. 7, pp. 79–87). Meteorology Center of Japan Meteorological Agency Tech.

Hong, S.-Y., Noh, Y., & Dudhia, J. (2006). A new vertical diffusion package with an explicit treatment of entrainment processes. *Monthly Weather Review*, *134*(9), 2318–2341. https://doi.org/10.1175/MWR3199.1

Hu, J., Yussouf, N., Turner, D. D., Jones, T. A., & Wang, X. (2019). Impact of ground-based remote sensing boundary layer observations on short-term probabilistic forecasts of a tornadic supercell event. *Weather and Forecasting*, *34*(5), 1453–1476. https://doi.org/10.1175/waf-d-18-0200.1

Hu, J., Fierro, A. O., Wang, Y., Gao, J., & Mansell, E. R. (2020). Exploring the assimilation of GLM-derived water vapor mass in a cycled 3DVAR framework for the short-term forecasts of high-impact convective events. *Monthly Weather Review*, *148*(3), 1005–1028. https://doi.org/10.1175/MWR-D-19-0198.1

James, E. P., & Benjamin, S. G. (2017). Observation system experiments with the hourly updating rapid refresh model using GSI hybrid ensemble? Variational data assimilation. *Monthly Weather Review*, *145*(8), 2897–2918. https://doi.org/10.1175/MWR-D-16-0398.1

Jones, T. A., Wang, X., Skinner, P., Johnson, A., & Wang, Y. (2018). Assimilation of *GOES-13* imager clear-sky water vapor ($6.5\,\mu$m) radiances into a warn-on-forecast system. *Monthly Weather Review*, *146*(4), 1077–1107. https://doi.org/10.1175/MWR-D-17-0280.1

Kim, D.-H., & Kim, H. M. (2018). Effect of assimilating Himawari-8 atmospheric motion vectors on forecast errors over East Asia. *Journal of Atmospheric and Oceanic Technology*, *35*(9), 1737–1752. https://doi.org/10.1175/JTECH-D-17-0093.1

Kim, M., Kim, H. M., Kim, J., Kim, S.-M., Velden, C., & Hoover, B. (2017). Effect of enhanced satellite-derived atmospheric motion vectors on numerical weather prediction in East Asia using an adjoint-based observation impact method. *Weather and Forecasting*, *32*(2), 579–594. https://doi.org/10.1175/WAF-D-16-0061.1

Lai, A., Gao, J., Koch, S. E., Wang, Y., Pan, S., Fierro, A. O., et al. (2019). Assimilation of radar radial velocity, reflectivity, and pseudo–water vapor for convective-scale NWP in a variational framework. *Monthly Weather Review*, *147*(8), 2877–2900. https://doi.org/10.1175/MWR-D-18-0403.1

Le Marshall, J., Seecamp, R., Dunn, M., Velden, C., Wanzong, S., Puri, K., et al. (2008). Shorter contribution the contribution of locally generated MTSat-1R atmospheric motion vectors to operational meteorology in the Australian region. *Australian Meteorological Magazine*, *57*, 359–365.

Lean, K., & Bormann, N. (2019). *Moving to GOES-16: A new generation of GOES AMVs*(EUMETSAT/ECMWF Fellowship Programme Research Report No. 49). Retrieved from https://www.ecmwf.int/node/18860

Lean, K., Bormann, N., & Salonen, K. (2016). *Assessment of Himawari-8 AMV data in the ECMWF system* (EUMETSAT/ECMWF Fellowship Programme Research Reports No. 42). Retrieved from https://www.ecmwf.int/node/16972

Li, J., Li, J., Velden, C., Wang, P., Schmit, T. J., & Sippel, J. (2020). Impact of rapid-scan-based dynamical information from GOES-16 on HWRF hurricane forecasts. *Journal of Geophysical Research: Atmospheres*, *125*(3). https://doi.org/10.1029/2019JD031647

Lim, A. H. N., Jung, J. A., Nebuda, S. E., Daniels, J. M., Bresky, W., Tong, M., & Tallapragada, V. (2019). Tropical cyclone forecasts impact assessment from the assimilation of hourly visible, shortwave, and clear-air water vapor atmospheric motion vectors in HWRF. *Weather and Forecasting*, *34*(1), 177–198. https://doi.org/10.1175/WAF-D-18-0072.1

Mallick, S., & Jones, T. A. (2020). Assimilation of GOES-16 satellite derived winds into the warn-on-forecast system. *Atmospheric Research*, *245*, 105131. https://doi.org/10.1016/j.atmosres.2020.105131

Mansell, E. R., & Ziegler, C. L. (2013). Aerosol effects on simulated storm electrification and precipitation in a two-moment bulk microphysics model. *Journal of the Atmospheric Sciences*, *70*(7), 2032–2050. https://doi.org/10.1175/JAS-D-12-0264.1

Mansell, E. R., Ziegler, C. L., & Bruning, E. C. (2010). Simulated electrification of a small thunderstorm with two-moment bulk microphysics. *Journal of the Atmospheric Sciences*, *67*(1), 171–194. https://doi.org/10.1175/2009JAS2965.1

Mlawer, E. J., Taubman, S. J., Brown, P. D., Iacono, M. J., & Clough, S. A. (1997). Radiative transfer for inhomogeneous atmospheres: RRTM, a validated correlated-k model for the longwave. *Journal of Geophysical Research: Atmospheres*, *102*(D14), 16663–16682. https://doi.org/10.1029/97JD00237

Nebuda, S., Jung, J., Santek, D., Daniels, J., & Bresky, W. (2014). Assimilation of GOES-R atmospheric motion vectors in the NCEP global forecast system. *Presented at the 12th International Winds Workshop, Copenhagen, Denmark*. Retrieved from http://cimss.ssec.wisc.edu/iwwg/iww12/talks/02_Tuesday/1210_Nebuda_IWW12_June_2014.pdf

Otsuka, M., Kunii, M., Seko, H., Shimoji, K., Hayashi, M., & Yamashita, K. (2015). Assimilation experiments of MTSAT rapid scan atmospheric motion vectors on a heavy rainfall event. *Journal of the Meteorological Society of Japan. Ser. II*, *93*(4), 459–475. https://doi.org/10.2151/jmsj.2015-030

Pan, S., Gao, J., Stensrud, D. J., Wang, X., & Jones, T. A. (2018). Assimilation of radar radial velocity and reflectivity, satellite cloud water path, and total precipitable water for convective-scale NWP in OSSEs. *Journal of Atmospheric and Oceanic Technology*, *35*(1), 67–89. https://doi.org/10.1175/JTECH-D-17-0081.1

Purser, R. J., Wu, W.-S., Parrish, D. F., & Roberts, N. M. (2003). Numerical aspects of the application of recursive filters to variational statistical analysis. Part I: Spatially homogeneous and isotropic Gaussian covariances. *Monthly Weather Review*, *131*(8), 1524–1535. https://doi.org/10.1175//1520-0493(2003)131<1524:NAOTAO>2.0.CO;2

Rao, P. A., Velden, C. S., & Braun, S. A. (2002). The vertical error characteristics of GOES-derived winds: Description and experiments with numerical weather prediction. *Journal of Applied Meteorology*, *41*(3), 253–271. https://doi.org/10.1175/1520-0450(2002)041<0253:TVECOG>2.0.CO;2

Roberts, N. M., & Lean, H. W. (2008). Scale-selective verification of rainfall accumulations from high-resolution forecasts of convective events. *Monthly Weather Review*, *136*(1), 78–97. https://doi.org/10.1175/2007MWR2123.1

Roebber, P. J. (2009). Visualizing multiple measures of forecast quality. *Weather and Forecasting*, *24*(2), 601–608. https://doi.org/10.1175/2008WAF2222159.1

Salonen, K., Cotton, J., Bormann, N., & Forsythe, M. (2015). Characterizing AMV height-assignment error by comparing best-fit pressure statistics from the met office and ECMWF data assimilation systems. *Journal of Applied Meteorology and Climatology*, *54*(1), 225–242. https://doi.org/10.1175/JAMC-D-14-0025.1

Sawada, M., Ma, Z., Mehra, A., Tallapragada, V., Oyama, R., & Shimoji, K. (2019). Impacts of assimilating high-resolution atmospheric motion vectors derived from Himawari-8 on tropical cyclone forecast in HWRF. *Monthly Weather Review*, *147*(10), 3721–3740. https://doi.org/10.1175/MWR-D-18-0261.1

Schmit, T. J., Griffith, P., Gunshor, M. M., Daniels, J. M., Goodman, S. J., & Lebair, W. J. (2017). A closer look at the ABI on the GOES-R series. *Bulletin of the American Meteorological Society*, *98*(4), 681–698. https://doi.org/10.1175/BAMS-D-15-00230.1

Schmit, T. J., Gunshor, M. M., Menzel, W. P., Gurka, J. J., Li, J., & Bachmeier, A. S. (2005). Introducing the next-generation advanced baseline imager on GOES-R. *Bulletin of the American Meteorological Society*, *86*(8), 1079–1096. https://doi.org/10.1175/BAMS-86-8-1079

Sears, J., & Velden, C. S. (2012). Validation of satellite-derived atmospheric motion vectors and analyses around tropical disturbances. *Journal of Applied Meteorology and Climatology*, *51*(10), 1823–1834. https://doi.org/10.1175/JAMC-D-12-024.1

Selz, T., & Craig, G. C. (2015). Upscale error growth in a high-resolution simulation of a summertime weather event over Europe. *Monthly Weather Review*, *143*(3), 813–827. https://doi.org/10.1175/MWR-D-14-00140.1

Shenk, W. E. (1991). Suggestions for improving the derivation of winds from geosynchronous satellites. *Global and Planetary Change*, *4*(1), 165–171. https://doi.org/10.1016/0921-8181(91)90087-D

Skamarock, W., Klemp, J., Dudhia, J., Gill, D., Barker, D., Wang, W., et al. (2008). *A description of the advanced research WRF version 3 [Application/pdf] (p. 1002 KB)*. UCAR/NCAR. https://doi.org/10.5065/D68S4MVH

Smith, T. M., Lakshmanan, V., Stumpf, G. J., Ortega, K. L., Hondl, K., Cooper, K., et al. (2016). Multi-Radar Multi-Sensor (MRMS) severe weather and aviation products: Initial operating capabilities. *Bulletin of the American Meteorological Society*, *97*(9), 1617–1630. https://doi.org/10.1175/BAMS-D-14-00173.1

Velden, C., Lewis, W. E., Bresky, W., Stettner, D., Daniels, J., & Wanzong, S. (2017). Assimilation of high-resolution satellite-derived atmospheric motion vectors: Impact on HWRF forecasts of tropical cyclone track and intensity. *Monthly Weather Review*, *145*(3), 1107–1125. https://doi.org/10.1175/MWR-D-16-0229.1

Velden, C. S., & Bedka, K. M. (2009). Identifying the uncertainty in determining satellite-derived atmospheric motion vector height attribution. *Journal of Applied Meteorology and Climatology*, *48*(3), 450–463. https://doi.org/10.1175/2008JAMC1957.1

Wu, T.-C., Velden, C. S., Majumdar, S. J., Liu, H., & Anderson, J. L. (2015). Understanding the influence of assimilating subsets of enhanced atmospheric motion vectors on numerical analyses and forecasts of tropical cyclone track and intensity with an ensemble Kalman filter. *Monthly Weather Review*, *143*(7), 2506–2531. https://doi.org/10.1175/MWR-D-14-00220.1

Xiao, Q., Zou, X., Pondeca, M., Shapiro, M., & Velden, C. (2002). Impact of GMS-5 and GOES9 satellite-derived winds on the prediction of a NORPEX extratropical cyclone. *Monthly Weather Review*, *130*, 507–528. https://doi.org/10.1175/1520-0493(2002)130<0507:IOGAGS>2.0.CO;2

Yamashita, K. (2012). An observing system experiment of MTSAT rapid scan AMV using JMA meso-scale operational NWP system. Presented at the 11th International Winds Workshop, Auckland, New Zealand. Retrieved from https://www-cdn.eumetsat.int/files/2020-04/pdf_conf_p60_s4_15_yamashit_v.pdf

Yamashita, K. (2017). Assimilation of Himawari-8 atmospheric motion vectors into the numerical weather prediction systems of Japan Meteorological Agency (JMA). Presented at the Fifth AMS Symposium on the Joint Center for Satellite Data Assimilation, 97th AMS Annual Meeting. Retrieved from https://ams.confex.com/ams/97Annual/webprogram/Paper304768.html

Zhao, J., Gao, J., Jones, T., & Hu, J. (2021). Impact of assimilating high-resolution atmospheric motion vectors on convective scale short-term forecasts. Part I: Observing system simulation experiment (OSSE). *Journal of Advances in Modeling Earth Systems*, *13*, e2021MS002484. https://doi.org/10.1029/2021MS002484

Ziegler, C. L. (1985). Retrieval of thermal and microphysical variables in observed convective storms. Part 1: Model development and preliminary testing. *Journal of the Atmospheric Sciences*, *42*(14), 1487–1509. https://doi.org/10.1175/1520-0469(1985)042<1487:ROTAMV>2.0.CO;2